

Finite compressibility and strain hardening in elasto-plastic models of amorphous matter.

A. Elgailani,¹ D. Vandembroucq,² and C.E. Maloney¹

¹*Department of Mechanical and Industrial Engineering,
Northeastern University, Boston, Massachusetts 02115, USA*

²*PMMH, CNRS UMR 7636, ESPCI Paris, PSL University,
Sorbonne Université, Université Paris Cité, F-75005 Paris, France*

(Dated: March 25, 2026)

We study a mesoscopic elasto-plastic model of amorphous matter with varying dimensionless compression modulus, K/μ , where K and μ are the compression and shear moduli. We study both cyclic shear with amplitude Γ and forward steady shear. In cyclic shear, the terminal behavior is, in order of increasing Γ : i) trivially elastic, ii) hysteretic but with microscopically reversible limit cycles, iii) diffusive with no return to previously visited configurations. We show that the transition between i) and ii) at the onset point Γ_0 is determined by the so-called Eshelby back stress, σ_0 , which depends on the Poisson ratio. The result is that systems which are more compressible, with smaller K/μ , are effectively harder with a higher value of Γ_0 and a correspondingly larger regime of purely elastic behavior in cyclic loading. In forward shear, we show that σ_0 plays a similar role where lower K/μ results in a higher value of the steady state flow stress, σ_y . We show how increasing K/μ results in an increase in the amplitude of the stress *redistribution* after a local yielding event without resulting in a change in the net stress *relaxation* from the event and discuss how this is related to the assumptions which go into mean-field descriptions of amorphous solids. Another striking feature of the model is the emergence of a complex hardening behavior in the absence of any microscopic ad-hoc hardening parameters or rules. In particular, we observe a transition between a kinematic and an isotropic hardening behavior precisely at the shear cycling amplitude Γ_0 associated with the hysteresis transition. The enhanced plastic response for incompressible systems is also seen in amorphous alloys where it is usually attributed to excess free volume, while in the present model, it arises simply as a consequence of the dependence of the Eshelby backstress on the Poisson ratio. Our results should have important implications for amorphous metallic alloys or other glassy systems (such as colloidal glasses, emulsions, etc.) where K/μ can vary with composition, age, quench procedure, or mechanical processing history.

I. INTRODUCTION

The plastic response and yielding behavior of amorphous solids such as amorphous alloys, soft glasses (colloidal glasses, emulsions, pastes, foams, etc.), and dense granular matter is understood to be controlled by local shear transformations [1–8]. After a local shear transformation, the surrounding material is subjected to stress increments as in Eshelby’s inclusion problem [4, 9–11]. It is a well known result from Eshelby’s solution to the inclusion problem that after a transformation, an inclusion will find itself under a stress that opposes the transformation just incurred [1, 10–12]. In Eshelby’s solution, the entire stress field in general, and the stress on the inclusion in particular, will depend on the compressibility of the material, typically expressed in terms of the Poisson ratio, ν , or the ratio of compression modulus to shear modulus, K/μ . The higher the value of K/μ , the higher the resulting stress both in the inclusion and in the surrounding matrix for a given amplitude of plastic strain in the inclusion. This effect of finite compressibility is accounted for in Argon’s seminal work on shear transformations [1, 12] where the energy barrier for thermally activated stress-biased shear transformations depends quantitatively on the Poisson ratio. However, somewhat surprisingly, quantitative accounting for finite compressibility is missing from most recent treatments of amorphous matter based on local shear transformations.

At the same time, it is well known that the Poisson ratio is empirically related to the ductility of amorphous alloys. In general, metallic glasses with high K/μ are more ductile with

higher fracture toughness [12]. Various authors interpret the result in slightly different terms [13–16], but broadly speaking, a high value of K/μ indicates that it is relatively easy to trigger shear-induced plastic relaxation and relatively difficult to cavitate and nucleate fracture. One might also expect the low values of μ/K in ductile systems to be related to excess low-lying soft modes in the system both associated with reduction in *shear* modulus and acting as modes for plastic relaxation [17–21]. However, a quantitative understanding of this relationship between K/μ and ductility is lacking.

In this work, using an elasto-plastic automaton based on a space-filling tiling of identical potential shear transformation sites, we show how the increasingly negative Eshelby back stress, σ_0 , and the associated larger redistribution of stresses at increasing values of K/μ allows systems to yield earlier at lower stresses and strains both in cyclic shear and in steady forward shear. In [22], we studied the cycling amplitude, Γ_0 , required to observe plastic hysteresis in the terminal steady states for an incompressible system. Here, in the compressible systems, we show we show that while σ_0 depends on K/μ , the previous Γ_0 dependence on σ_0 is in complete agreement with our previous work [22]. In the case of forward steady shear, we must slightly modify our scaling arguments based on σ_0 , but we arrive at a prediction for σ_y that differs quantitatively from the prediction for Γ_0 , although it has the same overall trend.

Amorphous systems subject to forward-reverse shear cycling have been the focus of an increasing number of experimental, theoretical, and numerical studies over the past several years [23–47]. In their seminal work [29], Keim and cowork-

ers identified three steady state response regimes for an amorphous material under cyclic shearing: at low amplitudes, the material eventually becomes elastic with no rearrangement of particles or atoms. At intermediate amplitudes, the material locks into limit cycles [39] with energy dissipating plastic rearrangements that precisely reverse themselves after an integer number of strain cycles to bring the system back to a previously visited microscopic configuration. At large amplitudes, the particle trajectories are diffusive, and the system never returns to any previous microscopic configuration. These three regimes define two transitions: the *hysteresis* transition from the elastic regime (ER) to the reversible plastic regime (RPR) at the amplitude Γ_0 , and the *irreversibility* transition from the RPR to the diffusive regime (DR) at the amplitude Γ_y where $\Gamma_y > \Gamma_0$.

Most works in the literature on forward-reverse cycling have focused on the later irreversibility transition at Γ_y , while the earlier hysteresis transition at Γ_0 has only been studied more recently. In reference [46], some of us studied an automaton elastoplastic model—based on the idea of tiling space with sites any of which could undergo a discrete plastic transformation according to the Eshelby theory [10]—and reproduced the three regimes. That work focused on the later transition, the irreversibility transition, at Γ_y . Later, in reference [22], we focused on the earlier transition, the hysteresis transition, at Γ_0 . We showed that while increasing the strain amplitude in the ER results in a harder terminal state with lower energy (analogous to the case with thermal annealing), increasing the strain amplitude in the RPR results in a softer material, with a lower plasticity onset strain γ_* , despite the fact that the energy continues to decrease with increasing amplitude. In our model, there is a characteristic value of stress, σ_0 , that a site will find itself under after it reaches the plastic threshold and transform; a so-called back stress. We found that σ_0 manifests itself as a characteristic feature in the stress distribution that determines γ_* and its dependence on Γ . We showed that Γ_0 is linked to σ_0 by the relation: $\Gamma_0 = \frac{1+\sigma_0/\mu}{2}$. We finally showed that Γ_0 corresponded to a state that is optimally hardened.

Here we extend these results to the case of finite compressibility. We discuss both oscillatory shear driving and forward shear driving. For the parts of this work concerning shear cycling, we continue to focus on the hysteresis transition at Γ_0 using the same model as in reference [22], but here, we allow for a finite compression modulus and investigate its effect. The only adjustable material parameter in our study is the dimensionless compressibility, K/μ , where K is the compression modulus and μ is the shear modulus. We find that Γ_0 increases as we decrease K/μ . Apart from that, everything we found in our previous study [22] continues to hold for a material with finite compressibility. For instance: 1) We show that the relation $\Gamma_0 = \frac{1+\sigma_0/\mu}{2}$ is maintained. However, now σ_0 depends on K/μ . 2) The plastic strain, ε , vs. the total strain, γ , curves have the same shape in [22] where above Γ_0 the plastic strain rate, $\frac{d\varepsilon}{d\gamma}$, jumps to a finite value of roughly 0.2 at γ_* independent of Γ or K/μ . 3) Below Γ_0 , the dissipated energy and the plastic strain are precisely zero but above Γ they continuously increase with Γ from zero

with the plastic strain amplitude ε_p following a powerlaw with $\varepsilon_p \propto (\Gamma - \Gamma_0)^{1.2 \pm 0.1}$. 4) Both γ_* and the stress value at γ_* , σ_* , decrease with Γ indicating a softening effect beyond Γ_0 and the relation $\gamma_* = \Gamma_0 - (\Gamma - \Gamma_0)$ is conserved. 5) σ_0 gives rise to a characteristic, Γ independent feature in the stress distribution $P(\sigma)$ that explains the nontrivial dependence of γ_* , σ_* and ε_p on Γ .

For forward shear, the situation is slightly more subtle. We show that for all K/μ , the $P(\sigma)$ distributions in steady state show a pronounced shoulder at σ_0 . After rescaling the distributions to take into account the K/μ dependent σ_0 , they show an almost perfect collapse. This allows us to express the dependence of the average flow stress in steady state, σ_y , in terms of σ_0 . This dependence of σ_y on σ_0 turns out to be qualitatively similar to but quantitatively different from the Γ_0 dependence on σ_0 . Both σ_y and Γ_0 decrease with increasing K/μ .

In the following we first discuss in section II the effect of finite compressibility on the Eshelby stress field induced by a plastic inclusion and detail the numerical discretization of the linear elasticity equations and stress equilibrium. In section III we present the mesoscopic elastoplastic model. Then we discuss the effect of finite compressibility on cyclic loading behavior in section IV. In particular we show that the material becomes increasingly ductile as the compressibility decreases – with the incompressible state being maximally ductile – and relate this trend to the dependence of the stress redistribution kernel on K/μ . In section V we discuss the forward shear loading behavior and analyze the decrease of the flow stress with decreasing compressibility; again indicating that the incompressible state is maximally ductile. In section VI, we explain the emergent hardening behavior in terms of simple schematic hardening model. We finally summarize and discuss our main results in section VII.

II. ESHELBY INCLUSIONS: EFFECT OF COMPRESSIBILITY ON CONTINUUM SOLUTION AND STAGGERED GRID DISCRETIZATION

A. Continuum solution

When an inclusion inside an initially stress free material undergoes a plastic transformation with a plastic strain ε_{ij} , known as the eigenstrain, the inclusion and the surrounding material will exert equal and opposite forces against each other. The Eshelby problem is to find the resulting displacement, u_i , its gradient, the linear strain, $\gamma_{ij} = \partial_i u_j$, and the resulting stress, σ_{ij} in both the transformed inclusion and the matrix. For an elliptical inclusion with homogeneous plastic strain, Eshelby showed that the total strain (also the stress) inside the inclusion is also spatially homogeneous. The Eshelby tensor, S_{ijkl} , relates the total strain inside the inclusion to the prescribed plastic strain:

$$\gamma_{ij} = S_{ijkl} \varepsilon_{kl}. \quad (1)$$

The solution for a circular inclusion in an infinite linear elastic medium is provided in [10] as:

$$S_{ijkl} = \frac{\lambda - \mu}{4\lambda + 8\mu} \delta_{ij} \delta_{kl} + \frac{\lambda + 3\mu}{4\lambda + 8\mu} (\delta_{ik} \delta_{jl} + \delta_{il} \delta_{jk}), \quad (2)$$

where the linear elastic material has an energy density, $\frac{1}{2} C_{ijkl} (\gamma - \varepsilon)_{ij} (\gamma - \varepsilon)_{kl}$, and the isotropic C tensor is described by the shear modulus, μ and Lamé parameter, λ : $C_{ijkl} = \lambda \delta_{ij} \delta_{kl} + \mu (\delta_{ik} \delta_{jl} + \delta_{il} \delta_{jk})$. Note the compression modulus, K , in 2D is $K = \lambda + \mu$. In this article, we use the three components of Voigt notation for γ , and ε , tensors referring to them as modes 1, 2, and 3 defined as:

$$\gamma_1 = \gamma_{xx} - \gamma_{yy}, \quad (3)$$

$$\gamma_2 = \gamma_{xy} + \gamma_{yx}, \quad (4)$$

$$\gamma_3 = \gamma_{xx} + \gamma_{yy}, \quad (5)$$

$$\varepsilon_1 = \varepsilon_{xx} - \varepsilon_{yy}, \quad (6)$$

$$\varepsilon_2 = \varepsilon_{xy} + \varepsilon_{yx}, \quad (7)$$

$$\varepsilon_3 = \varepsilon_{xx} + \varepsilon_{yy}. \quad (8)$$

It then follows that the σ_α are given by

$$\sigma_1 = (\sigma_{xx} - \sigma_{yy})/2, \quad (9)$$

$$\sigma_2 = (\sigma_{xy} + \sigma_{yx})/2, \quad (10)$$

$$\sigma_3 = (\sigma_{xx} + \sigma_{yy})/2. \quad (11)$$

In this study, we shear the system in mode 2 so we are mainly interested in its corresponding quantities. So we have: $\varepsilon_{xx} = \varepsilon_{yy} = 0$ and $\varepsilon_{xy} = \varepsilon_{yx} = \frac{1}{2}$ which gives $\varepsilon_2 = \varepsilon_{xy} + \varepsilon_{yx} = 1$ and, following equation 2, $\gamma_2 = \gamma_{xy} + \gamma_{yx} = \frac{\lambda + 3\mu}{2\lambda + 4\mu}$. The stress in the circular inclusion, the constrained stress, σ_c , is proportional only to the elastic part of the strain, so we have $\sigma_c = \mu(\gamma_2 - \varepsilon_2) = \mu(\gamma_2 - 1)$ which gives:

$$\sigma_c = -\frac{\mu}{2} \frac{\lambda + \mu}{\lambda + 2\mu} = -\mu \frac{\alpha}{4}, \quad (12)$$

where we have defined the dimensionless combination of Lamé parameters:

$$\alpha = 2 \frac{\lambda + \mu}{\lambda + 2\mu} = 2 \frac{K}{K + \mu}. \quad (13)$$

Note that the negative sign in equation 12 indicates that the inclusion experiences a shear stress in the opposite direction to the positive plastic strain ε_2 that was prescribed. The amplitude of this constrained stress is controlled by the dimensionless parameter α , which, at fixed μ , monotonically increases with the compression modulus, K , and saturates at $\alpha = 2$ for incompressible materials.

It is important to note that, by symmetry, we would obtain precisely the same constrained stress for any orientation of the shear: be it in mode-1 with $\varepsilon_1 = 1$, mode-2 with $\varepsilon_2 = 1$, or any combination of them. Furthermore, if we impose an eigenstrain with pure shear and no dilatancy, so that $\varepsilon_3 = 0$, then there will be no resulting dilatant strain, so γ_3 will be zero. Finally, and most importantly, in the *continuum* solution

presented here for *an infinite medium without a boundary*, the entire solution both inside the inclusion and in the matrix for mode-2 will be precisely equal to the solution for mode-1 rotated by 45 degrees and vice versa. The solution in a periodic square cell discretized with finite differences on a square grid presented below will break this symmetry in subtle ways and mode-1 and mode-2 will be closely related to each other but not precisely equivalent as they are in the infinite continuum.

B. Staggered grid discretization

In our discretization of the Eshelby problem, a 2D material is divided into square tiles, and the total energy, U , is defined as the sum of the local energies of the tiles. That is: $U = \sum_{I,J} U[I,J]$, where I and J are the spatial indices of the tiles with $0 \leq I < L$ and $0 \leq J < L$. The total strain at a tile, $\gamma[I,J]$, is additively decomposed into an elastic part, $\varepsilon_e[I,J]$, and a plastic part, $\varepsilon[I,J]$, where the plastic part is to be identified with the eigenstrain in the continuum Eshelby problem. So we have:

$$\gamma_1[I,J] = \varepsilon_{e1}[I,J] + \varepsilon_1[I,J]. \quad (14)$$

We define the local energy using only the elastic strain:

$$U[I,J] = \frac{\mu}{2} ((\gamma_1[I,J] - \varepsilon_1[I,J])^2 + (\gamma_2[I,J] - \varepsilon_2[I,J])^2) + \frac{K}{2} (\gamma_3[I,J])^2. \quad (15)$$

So then the shear stress for modes 1 and 2, $\sigma[I,J]$, is:

$$\sigma[I,J] = \mu \varepsilon_e[I,J] = \mu (\gamma[I,J] - \varepsilon[I,J]). \quad (16)$$

The discretized Eshelby problem is then to find the total strain, γ , and the displacement, u , from which it was derived, that minimize U for a given ε . To obtain γ from u , we use the so-called staggered difference scheme [48–53]:

$$\begin{aligned} \gamma_{xx}[I,J] &= u_x[I+1,J] - u_x[I,J], \\ \gamma_{xy}[I,J] &= u_y[I,J] - u_y[I-1,J], \\ \gamma_{yx}[I,J] &= u_x[I,J] - u_x[I,J-1], \\ \gamma_{yy}[I,J] &= u_y[I,J+1] - u_y[I,J]. \end{aligned} \quad (17)$$

We put 17 into 15 and solve for the u that minimizes the energy and then substitute the solution, u , into 17 to get the strain from which we can find the stress by using 16. This is completely equivalent to minimizing the total energy with respect to the total strain field *subject to the constraint that the total strain field be kinematically compatible* – i.e. *be the derivative of a displacement field*. The staggered grid scheme implicitly defines the notion of kinematic compatibility. To find the so-called Eshelby kernel, $G[I,J]$, we consider the special case where the prescribed $\varepsilon[I,J]$ is the discrete delta function: $\varepsilon[I,J] = \delta_{I0} \delta_{J0}$. Let $G_{\alpha\beta}$ be the α -th Voigt strain resulting from an imposed eigenstrain in mode β . So then G_{11} is the γ_1 strain resulting from an imposed ε_1 eigenstrain, G_{12} is the γ_1 strain resulting from an imposed ε_2 eigenstrain, G_{21} is the

γ_2 strain resulting from an imposed ε_1 eigenstrain, and G_{22} is the γ_2 strain resulting from an imposed ε_2 . We use a staggered grid scheme here as using a second order centered difference scheme gives pathological behavior for G_{12} and G_{21} , however, the results for G_{11} and G_{22} are equivalent to what one would obtain in a second order centered difference scheme. To solve for G , it is easiest to work in Fourier space.

We use the following Fourier transform conventions [54].

$$f[I, J] = \frac{1}{L^2} \sum_{m,n=0}^{L-1} \tilde{f}[m, n] \exp[-i2\pi(Im + Jn)/L] \quad (18)$$

where:

$$\tilde{f}[m, n] = \sum_{I,J=0}^{L-1} f[I, J] \exp[+i2\pi(Im + Jn)/L] \quad (19)$$

After differentiating the total energy with respect to the displacement field and performing some algebra to solve for the energy minimum, we obtain \tilde{G} :

$$\tilde{G}_{11}[m, n] = \frac{2\lambda + 3\mu}{\lambda + 2\mu} \tilde{A}[m, n] + \frac{\mu}{\lambda + 2\mu} \tilde{B}[m, n] \quad (20)$$

$$\tilde{G}_{21}[m, n] = -\frac{2(\lambda + \mu)q_{x-}q_{y-}(\Delta_x^2 - \Delta_y^2)}{(\lambda + 2\mu)\mathcal{D}} \quad (21)$$

$$\tilde{G}_{12}[m, n] = -\frac{2(\lambda + \mu)q_{x+}q_{y+}(\Delta_x^2 - \Delta_y^2)}{(\lambda + 2\mu)\mathcal{D}} \quad (22)$$

$$\tilde{G}_{22}[m, n] = -\frac{\lambda}{\lambda + 2\mu} \tilde{A}[m, n] + \tilde{B}[m, n] \quad (23)$$

for $(m, n) \neq (0, 0)$ and $\tilde{G}[0, 0] = 0$. Setting $\tilde{G}[0, 0] = 0$ simply fixes the spatial average of the strain to be 0. A non-zero average strain would shift the total energy but not change the displacement field which minimizes it. Furthermore, any strain field defined by the staggered grid procedure in equations 17 must have zero spatial average if the boundaries of the periodic cell are assumed to be held fixed, and this condition is not implied by the algebra in Fourier space and must be specified separately. Here: (m, n) are Fourier indices;

$$\Delta_x^2 = q_{x+}q_{x-} \quad (24)$$

$$\Delta_y^2 = q_{y+}q_{y-} \quad (25)$$

are the Fourier transforms of the second ordered centered difference operators in the x and y direction;

$$\mathcal{D} = (\Delta_x^2 + \Delta_y^2)^2 \quad (26)$$

is the Fourier transform of the bi-Laplacian. We have defined:

$$\tilde{A}[m, n] = \frac{2\Delta_x^2\Delta_y^2}{\mathcal{D}} \quad (27)$$

$$\tilde{B}[m, n] = \frac{\Delta_x^4 + \Delta_y^4}{\mathcal{D}} \quad (28)$$

for $(m, n) \neq (0, 0)$ and $\tilde{A} = 0, \tilde{B} = 0$ for $(m, n) = (0, 0)$ so that $\tilde{G}[0, 0] = 0$ to have zero average total strain in real space. The

$q_{x\pm}$ and $q_{y\pm}$ are the Fourier transforms of the forward and backward difference operators in the x and y directions [53]

$$q_{x+}[m, n] = -i(+\exp[+2\pi im/L] - 1) \quad (29)$$

$$q_{x-}[m, n] = -i(-\exp[-2\pi im/L] + 1) \quad (30)$$

$$q_{y+}[m, n] = -i(+\exp[+2\pi in/L] - 1) \quad (31)$$

$$q_{y-}[m, n] = -i(-\exp[-2\pi in/L] + 1) \quad (32)$$

In the continuum Eshelby problem of a circular inclusion in an infinite linear elastic medium, there is a high degree of symmetry which is only approximate in the present model where the symmetry is broken both by the square periodic cell and the discrete square tiling. In the infinite continuum result, the G_{11} and G_{22} fields can be obtained from each other simply by a 45-degree rotation. In the equivalent continuum calculation, one would have $\tilde{A} = 2\Delta_x^2\Delta_y^2/\mathcal{D} \rightarrow 2\cos^2(\theta)\sin^2(\theta)$ and $\tilde{B} = (\Delta_x^4 + \Delta_y^4)/\mathcal{D} \rightarrow \cos^4(\theta) + \sin^4(\theta)$ where θ is the angle of the wavevector in the x, y plane. One would then have: $\tilde{A} + \tilde{B} = 2\cos^2(\theta)\sin^2(\theta) + \cos^4(\theta) + \sin^4(\theta) = 1$. In the present discrete square-cell case, $\tilde{A}[m, n]$ and $\tilde{B}[m, n]$ are related by:

$$\tilde{A}[m, n] + \tilde{B}[m, n] = 1 - \delta_{m0}\delta_{n0} \quad (33)$$

In other words, \tilde{A} and \tilde{B} sum to 1 at every point in Fourier space except the origin. So in real space

$$A[I, J] + B[I, J] = \delta_{I0}\delta_{J0} - \frac{1}{L^2} \quad (34)$$

Substituting 33 into 20 and 23 and recalling the definition of α from equation 13, we get

$$\tilde{G}_{11}[m, n] = \alpha\tilde{A}[m, n] + \frac{\mu(1 - \delta_{m0}\delta_{n0})}{\lambda + 2\mu} \quad (35)$$

$$\tilde{G}_{22}[m, n] = -\alpha\tilde{A}[m, n] + (1 - \delta_{m0}\delta_{n0}) \quad (36)$$

in Fourier space, and in real space

$$G_{11}[I, J] = \alpha A[I, J] + \frac{\mu(\delta_{I0}\delta_{J0} - \frac{1}{L^2})}{(\lambda + 2\mu)} \quad (37)$$

$$G_{22}[I, J] = -\alpha A[I, J] + \delta_{I0}\delta_{J0} - \frac{1}{L^2} \quad (38)$$

This implies that as $L \rightarrow \infty$, other than precisely at the origin, $G_{11} \approx -G_{22} \approx \alpha A[I, J]$. G_{11} is precisely equal to $-G_{22}$ in the continuum solution, whereas here it is only approximate and involves a correction term of order $1/L^2$ which is related to the boundary conditions in the discrete finite system that G have zero spatial average.

In figure 1, we show G_{11} and G_{22} in real space near the origin for $\lambda/\mu = 4$ for a system of size $L = 128$. Note that they are approximately equal in magnitude but opposite in sign other than at the origin, as in the continuum case. However, the square lattice breaks the invariance under rotation by $\pi/4$ enjoyed by the continuum solution.

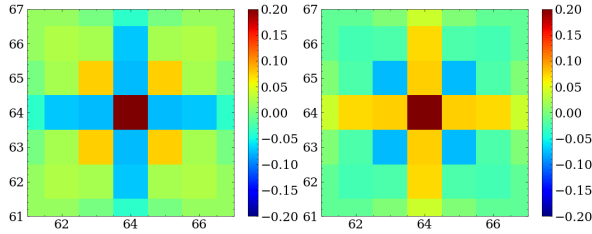


FIG. 1. The real space G_{11} (left) and G_{22} (right) near the origin for a system of size $L = 128$ and $\lambda/\mu = 4$. Other than at the origin, $G_{11} = -G_{22}$ apart from a correction term which vanishes as $1/L^2$.

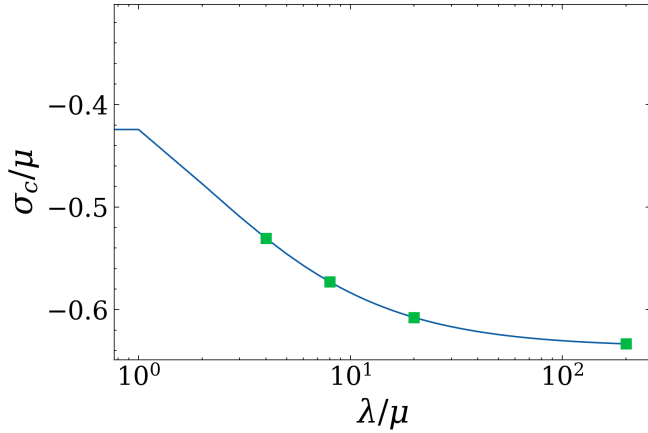


FIG. 2. The constrained stress σ_c in mode-2 vs. λ/μ . The squares are the discretized solution for a system size $L = 128$. The solid line is the continuum solution (multiplied by $4A[0,0] = 1.2732$) for a circular inclusion in an infinite medium.

The constrained stress, σ_c , in the Eshelby problem is obtained by subtracting off the plastic piece, $\varepsilon[0,0] = 1$, from the total strain at the origin and multiplying by μ . So for mode-2:

$$\sigma_c = \mu(G_{22}[0,0] - 1) \quad (39)$$

$$= -\mu \left(\alpha A_0 + \frac{1}{L^2} \right) \quad (40)$$

where

$$A_0 = A[0,0] \quad (41)$$

(A similar calculation for mode-1 gives: $\sigma_c = -\mu\alpha(1 - 2A_0)/2 + \mathcal{O}(1/L^2)$.) If we neglect the $1/L^2$ terms, we see that σ_c has the same dependence on the Lamé parameters as in the continuum case. In mode-2, σ_c is $4A_0 \approx 1.2732$ times the continuum-disk result, while in mode-1, σ_c is $4(1/2 - A_0) \approx 1.4536$ times the continuum-disk result. In figure 2, we plot the discretized σ_c in mode-2 (equation 40) for $L = 128$ and the continuum σ_c for a circular inclusion (equation 12) multiplied by a prefactor of $4A_0$. For convenience, we have defined the particular dimensionless ratio of elastic moduli which emerges from the continuum Eshelby calculation as α ; it is the only combination of elastic moduli that will enter into our elasto-plastic model specified below. α grows monotonically from zero at $K/\mu = 0$ (a maximally negative Poisson

ratio, completely compressible material) to 2 at $\mu/K = 0$ (an incompressible material).

σ_c is negative which reflects the fact that, in the canonical Eshelby problem where the matrix and inclusion are both initially stress-free before the transformation – after the transformation, the inclusion feels a stress from the matrix pushing it backwards away from its new stress-free configuration at $\gamma = 1$ where the stress would be zero. Since σ_c is negative and a decreasing function of λ/μ , its *magnitude* increases. This indicates larger surface tractions applied by the matrix to constrain the inclusion. As we will see below, these larger backward stresses in the Eshelby problem lead to macroscopic yielding behavior at lower values of applied strain and stress despite the fact that the elementary yield strain of the local elements is held fixed in the model.

III. MODEL

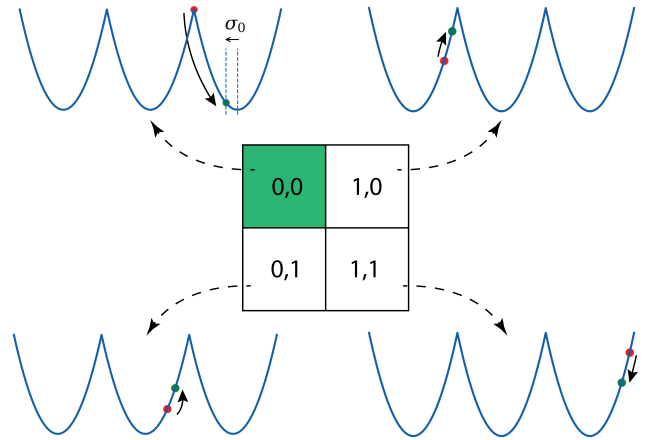


FIG. 3. A schematic of a single elementary shear transformation in the automaton at a site $[0,0]$, and the resulting changes in local strain and energy in a few nearby sites on the grid after re-equilibration. The parabolas show the local energy, U , of the sites as a function of the total strain, γ . The center of the n -th parabola is at $\gamma = 2n$, and the transition between basin n and basin $n \pm 1$ occurs at $\gamma = 2n \pm 1$. The stress, σ , as a function of total strain, γ , is then $\sigma = \gamma - 2F[\frac{\gamma}{2} + \frac{1}{2}]$ where F is the floor function defined in the text. The four different identical landscapes correspond to the four different tiles shown. The red and green dots indicate local strain values before and after a shear transformation at the site labeled $[0,0]$. After the transformation, sites $[1,0]$ and $[0,1]$ are at a higher energy and stress, site $[1,1]$ is at a lower energy and stress, while the transforming site, site $[0,0]$, is at a much lower – but non-zero – energy and at a *negative* stress.

To implement an elasto-plastic model, we suppose that any site in the material has the same piecewise quadratic strain-energy function as given by equation 15, but where the plastic shear strain, $\varepsilon_{1(2)}$, is determined self-consistently to connect the parabolas.

$$\varepsilon_{1(2)} = 2F \left[\frac{\gamma_{1(2)}}{2} + \frac{1}{2} \right] \quad (42)$$

where $F[x]$ is the floor function that returns the greatest integer less than or equal to x . This construction gives parabolas which each range from $\gamma = 2n - 1$ to $\gamma = 2n + 1$ with transitions from one parabola to the next occurring at $\gamma = 2n \pm 1$ (figure 3). Since the minima are separated by a strain of 2, the plastic strain increment in the model must be 2 as reflected in the prefactor of 2 on the floor function.

This sets the microscopic condition for yielding (a transition from one parabola to the next) as $\gamma - \varepsilon = \pm 1$, and, implicitly this sets the microscopic yield strain to unity. All quantities with units of strain emerging from the model should be understood to be measured in units of this microscopic yield strain. We also set $\mu = 1$ and measure all stresses and λ and K in units of μ . This piecewise-quadratic strain energy function then gives a single-valued Hamiltonian for the system which depends on the displacement field implicitly via the total strain and is piece-wise quadratic in the displacement field. The discretized Eshelby solution then provides a way to find and enumerate energy minima of this Hamiltonian.

To use the Hamiltonian to define an evolution protocol for an integer automaton we proceed as follows: i) For a given γ and ε , increment (or decrement) ε by 2 in all the sites with $|\gamma - \varepsilon| > 1$ and, simultaneously, update γ everywhere in accordance with the discretized Eshelby solution. ii) Repeat (i) until all sites are below threshold with $|\gamma - \varepsilon| < 1$. At this point, the γ field will be the derivative of a displacement field which minimizes the total Hamiltonian, and, as such will automatically be compatible. iii) Advance the imposed total strain homogeneously until one site is precisely at threshold with $|\gamma - \varepsilon| = 1$. iv) Repeat. We initialize the systems by adding a random plastic field of ± 2 at each site (in both mode 1 and mode 2) and running the automaton evolution. We have checked that repeating this initialization process again on a previously initialized configuration does not affect our results qualitatively, and our initial state should be thought of as a rapidly quenched glass from a high temperature liquid with a high degree of disorder.

The stress increment at site $[I, J]$ due to a transformation at site $[K, L]$ is given by:

$$\Delta\sigma[I, J] = -2\alpha A[K - I, L - J] - \frac{2}{L^2} \quad (43)$$

This expression is valid for any site in the system *including the transforming site itself*. If we recall that $\sum_{IJ} A[I, J] = 0$ by construction, this makes it clear that there is a quantum of stress relaxation associated with a single transformation in our model: $\Delta\sigma = -2/L^2$ which is independent of α . Here, σ with no lattice indices refers to the spatial average: $\sigma = \frac{1}{L^2} \sum_{IJ} \sigma[I, J]$. It is only the amplitude of stress redistribution, rather than the quantum of relaxation, which depends on α , and it is, in fact, simply proportional to α . A word of caution is appropriate here: the $\Delta\sigma[I, J]$ defined in equation 43 excludes the $\delta_{IK}\delta_{JL}$ which appears in equation 38, as we must subtract off the plastic strain arising in the Eshelby problem to obtain the elastic strain at the origin.

In figure 3, we show a schematic of a single elementary shear transformation at a site $[0, 0]$. In the figure, we show only the transforming site and three neighboring sites, but it is

to be understood that the transformation will affect the strain values at all sites in the plane. Suppose that, initially, site $[0, 0]$ is at the threshold as we are loading the system in the positive direction. The total strains at the sites before the transition are indicated by the red dots. The location of all the red dots corresponds to an energy minimum of the Hamiltonian. The red dots need not all be in the same basin; i.e. there may be plastic strain in the system, and local values of strain are determined by the values of the plastic strain throughout the entire system. As site $[0, 0]$ crosses $\gamma = 1$, the plastic strain, ε , will be incremented by 2. After the event, the new total strains (and stresses) at all sites will be incremented/decremented according to the Eshelby solution *including site $[0, 0]$ itself!* The updated strains are indicated by the green dots. At site $[0, 0]$, γ will be incremented and will be at the left half of the next parabola. The new stress at site $[0, 0]$ immediately after yielding, σ_0 , is the so-called back stress, and it sits at a negative value when the site yields in the forward direction. σ_0 is obtained from $2\sigma_c$ by adding 1 since σ_c is the post-transformation stress at the transformed site in a system that is initially stress free:

$$\sigma_0 = 2\sigma_c + 1 = 1 - 2\alpha A_0 - \frac{2}{L^2} \quad (44)$$

The locations of the red and green dots in the figure are determined from the exact values for $\lambda = 200$ in a 128-by-128 system.

In our previous study [22], we showed, in the incompressible limit, that σ_0 gives rise to a characteristic shape of the stress distribution and we argued that it can be used to predict the location of Γ_0 . Here we show the same relation between σ_0 and Γ_0 follows for the finite compression modulus case, despite the dependence of σ_0 on K/μ . Furthermore, we show that a similar relation exists between σ_0 and σ_y , the steady state flow stress in steady-forward shear.

IV. CYCLIC LOADING

In this section, first we present the loading curves for systems of various compressibility subjected to cyclic shear. For cycling amplitudes below Γ_0 , the terminal loading curves are trivial with no hysteresis. For cycling amplitudes above Γ_0 , we show that the hysteretic loading curves have a quiescent period devoid of any significant plastic activity followed by a rapid initiation of plastic activity after the strain exceeds a level, γ_* , and we explain the dependence of γ_* on Γ_0 . Next, we relate the rapid onset of plasticity at γ_* to the form of the probability distribution of local stress values and explain how important features of that distribution are governed by the residual stress present at a local site after an Eshelby transformation. Finally, we show how the compressibility dependence of the residual stress in the Eshelby transformation perfectly accounts for the compressibility dependence of Γ_0 .

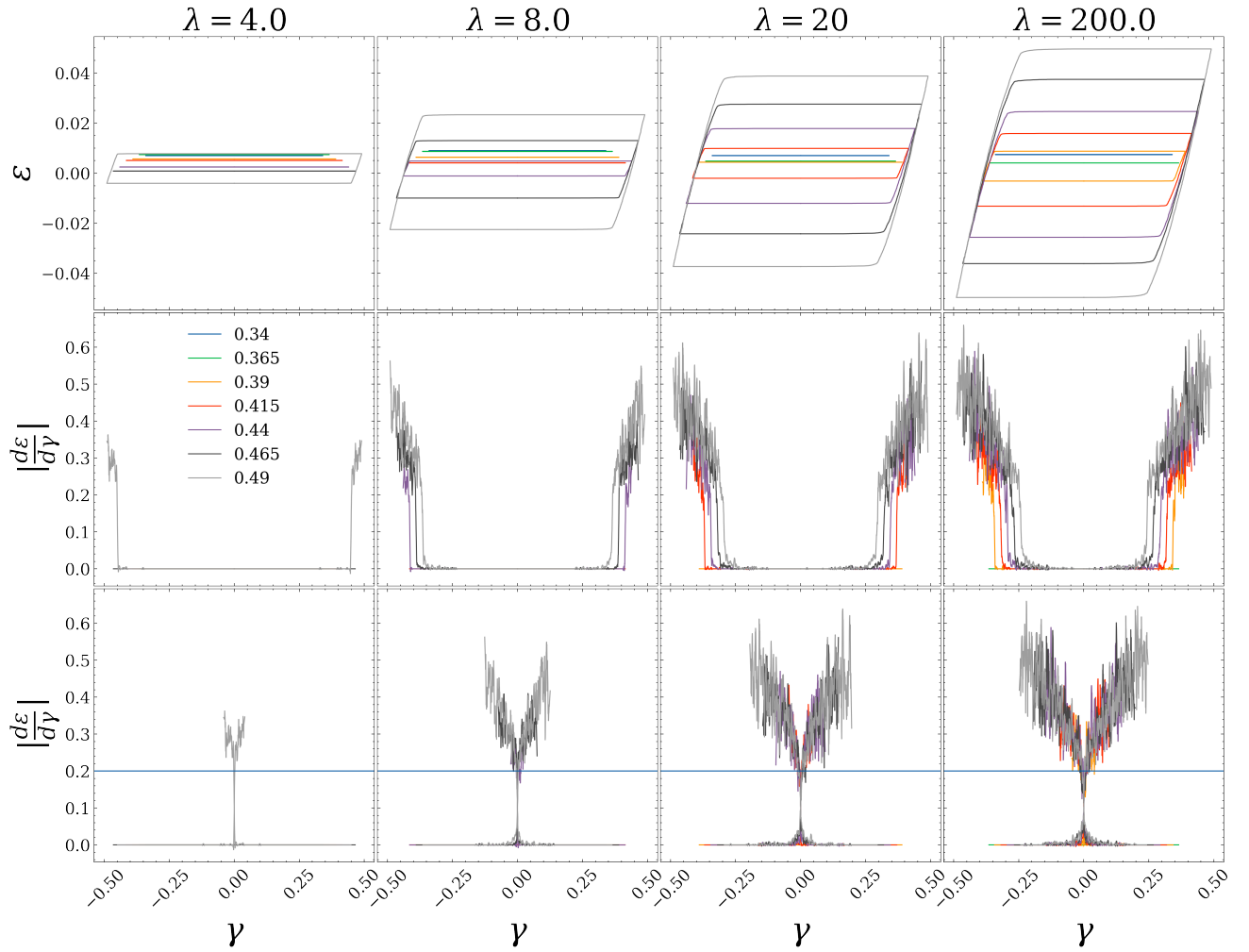


FIG. 4. Top row: plastic strain ε (ensemble average) in the limit cycles vs. strain γ for several different strain amplitudes Γ and four different values of Lamé parameter λ . Middle row: the strain rate $|\frac{d\varepsilon}{d\gamma}|$ vs γ for the curves in the top row. Bottom row: the strain rate $|\frac{d\varepsilon}{d\gamma}|$ vs $\gamma - \gamma_*$ for the curves in the top row where γ_* is the plasticity onset strain. The solid line in the bottom row is at $|\frac{d\varepsilon}{d\gamma}| = 0.2$

A. Strain and strain rate curves

In figure 4 (top), we show the ensemble average of the plastic strain, ε , in the terminal limit cycles—after the transient has died away— vs. the applied strain, γ , for several different cycling amplitudes, Γ , both below and above the transition value, Γ_0 , for different values of λ : 4, 8, 20, and 200.

We immediately notice the strong dependence of the hysteresis on the compressibility. Systems with larger λ (smaller compressibility), have larger hysteresis amplitude. For all λ values, for $\Gamma < \Gamma_0$, the system is in the ER, where after the transient, ε is a flat line with no plastic events or energy dissipation. The exact location of the residual ε , where the flat lines are located, is a non-trivial function of the cycling amplitude, Γ , but they all sit at a positive value. This symmetry breaking is a result of our arbitrary choice to load the virgin state in the forward direction first. For the smallest $\lambda = 4$ in our set, only the highest amplitude, $\Gamma = 0.49$, is in the RPR as indicated by the hysteretic ε vs. γ loop. As λ increases, hysteresis starts at lower Γ . For example, at $\lambda = 8.0$, there are three amplitudes in the RPR: 0.44, 0.465, and 0.49. Similarly, for $\lambda = 20$ and 200 we have, respectively, 4 and 5 amplitudes in the RPR. We discuss the location, Γ_0 , of the onset of hysteresis and its dependence on λ in the text below.

In figure 4 (middle), we plot the plastic strain rate, $|d\varepsilon/d\gamma|$. The strain rate curves all show a relatively sharp transition from zero to roughly 0.2 at a characteristic value of strain, γ_* , which depends on both λ and Γ . We define γ_* as the γ value for which the strain rate first exceeds 0.1, and we have checked that γ_* is not very sensitive to this precise choice as the jump in $\frac{d\varepsilon}{d\gamma}$ is rather sharp. In the bottom row, we shift the curves horizontally and show $|d\varepsilon/d\gamma|$ vs. $\gamma - \gamma_*$. After shifting, the curves can be seen to have roughly the same shape. While the size of the jump is independent of λ and Γ , the sharpness of the jump depends on $|\Gamma - \Gamma_0|$. The larger the $\Gamma - \Gamma_0$, the more rounded the transition is, with more plasticity occurring at $|\gamma| < \gamma_*$. This regime of small amounts of plasticity at $|\gamma| < \gamma_*$ is reminiscent of creep in other systems [55–59]. It is interesting to note that the systems which are cycled at Γ just slightly above Γ_0 have virtually no creep and no plasticity until a sudden burst of plasticity at the turning point $\gamma \approx \Gamma$ where the sense of the driving strain is reversed. For example, the gray curve on the left at $\lambda = 4, \Gamma = 0.49$ has virtually no plasticity until the sudden burst near the turning point at $\gamma \approx 0.49$.

B. Plasticity onset at γ_*

In figure 5 (top), we show the onset strain, γ_* in the limit cycles for different values of λ . We plot both γ_*^+ in the forward sense (crosses) and $-\gamma_*^-$ in the reverse sense (pluses). Below Γ_0 (the vertical lines), the systems are in the elastic regime where the limit cycles are trivial with no plasticity or energy dissipation and $\gamma_* = \Gamma$ in this case. At Γ_0 , the systems are maximally hardened. Above Γ_0 , γ_* follows an almost perfect line with $\gamma_* = \Gamma_0 - (\Gamma - \Gamma_0)$. It is apparent that for a fixed Γ ,

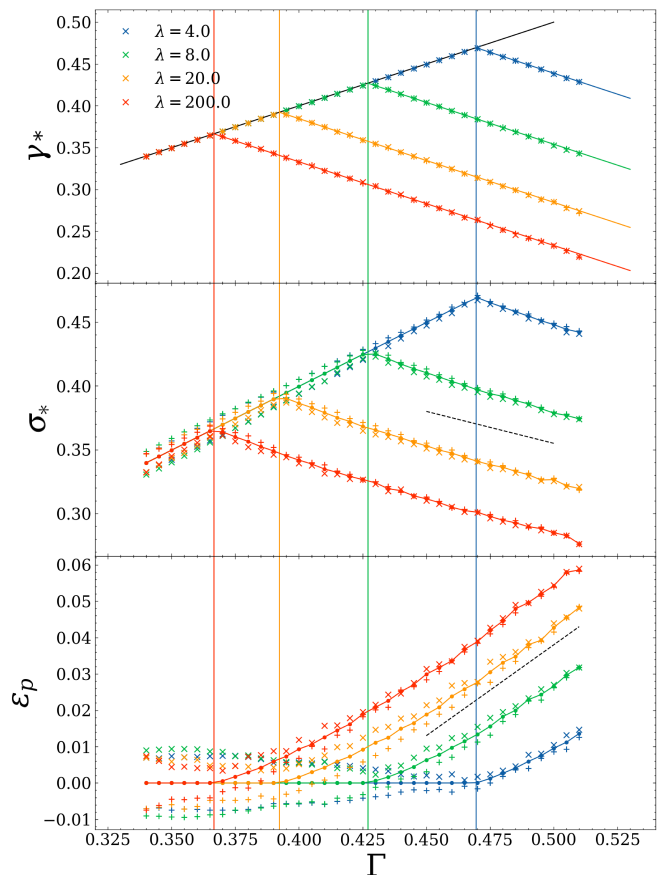


FIG. 5. Top row: The (negative) onset strain, $\pm\gamma_*^{+(-)}$, in the forward (and reverse) direction for different values of the first Lamé parameter λ . The solid lines are $\gamma_* = \Gamma_0 - (\Gamma - \Gamma_0)$ with Γ_0 determined by taking the average $(\Gamma + \gamma_*)/2$ for a given λ . Middle row: The (negative) stress at onset, $\pm\sigma_*^{+(-)}$, in the forward (and reverse) direction. The dashed line is a guide to eye with a slope = $-1/2$. Bottom row: The (negative) plateau strain, $\pm\varepsilon_p^{+(-)}$, in the forward (and reverse) direction. The dashed line is a guide to eye with a slope = $1/2$. The vertical lines are at Γ_0 for the different λ values. In all cases, the crosses and pluses are for the forward and reverse directions, respectively. The dots in b) and c) mark the averages.

γ_* decreases with increasing λ . What this means is that at a given Γ , systems with higher λ , which are less compressible, exhibit plasticity earlier in the cycle at smaller values of strain.

In figure 5 (middle), we show the stress at the forward plasticity onset (crosses), σ_*^+ , and the negative stress at the backward onset (pluses), $-\sigma_*^-$, along with their average (dots). Similarly, in figure 5 (bottom), we plot the plastic strain plateau value at the forward turning point (pluses), ε_p^+ , and the negative plateau value at the reverse turning point (pluses), $-\varepsilon_p^-$, along with their average (dots). The asymmetry we see in σ_* and ε_p in the middle and bottom rows, respectively, is the result of our choice to begin the simulation by pushing the system in the forward sense but it goes away for larger Γ . Similar to γ_* , in the RPR, σ_* decreases with Γ with $\frac{d\sigma_*}{d\Gamma}$ approaching a slope of $-1/2$ while ε_p increases from zero with $\frac{d\varepsilon_p}{d\Gamma}$ approaching a slope of $1/2$. We will explain the connec-

tion between the decrease in the yield stress and the increase in the hysteresis amplitude below in section VI, where we introduce a simplified, idealized description of the hardening behavior assuming a constant plastic strain rate and associated perfectly rhombic ε vs. γ and σ vs. γ curves.

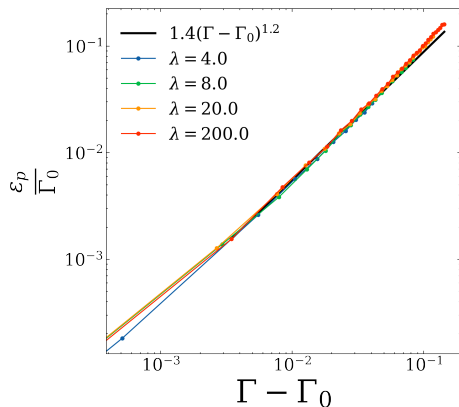


FIG. 6. The average of the forward and backward plateau strain ε_p vs. $\Gamma - \Gamma_0$ for different values of λ .

In figure 6, we plot the average of the forward and the backward values of plateau plastic strain, ε_p , as in figure 5 (bottom), but here we plot ε_p/Γ_0 vs. $\Gamma - \Gamma_0$. The data collapse almost perfectly onto a single master curve. The master curve is reasonably well represented by a power law with an exponent of 1.2 and a prefactor of 1.4 which is consistent with our result for the incompressible case [22]. It is not immediately obvious why one would need to scale ε_p by Γ_0 , but, empirically, it is necessary to obtain a good collapse.

C. Stress distribution

In figure 7 we plot the distribution of the local stress, $P(\sigma)$, at the forward turning point for several different values of Γ for the same set of λ as above. The vertical dashed lines are at the average. The vertical solid lines are located at $-1 + 2\Gamma$ and shown for only the elastic systems.

For systems in the ER, the distribution is symmetric about the average (dashed lines) which sits at a positive value because we show the forward turning point where the stress is positive. Because there is no plasticity for the systems in the ER as we strain them backward from $+\Gamma$ to $-\Gamma$, the distributions will simply shift horizontally to the left by 2Γ . This means that at the forward turning points, $P(\sigma)$ must be zero for $\sigma < -1 + 2\Gamma$ as indicated by the vertical solid lines. Otherwise, if $P(\sigma)$ was non-zero for some $\sigma < -1 + 2\Gamma$ then the system would exhibit some plasticity during reverse shear and therefore could not be elastic.

For all systems, both the elastic systems below Γ_0 and the reversible plastic systems above Γ_0 , a feature appears at σ_0 . For the elastic systems, the distribution has an excess above the background around σ_0 . The excess sites with $\sigma \approx \sigma_0$ presumably result from the last few forward strain sweeps during the transient before plasticity was extinguished. During these

sweeps, the sites which yielded just before the reversal point would have ended up with a final strain value of σ_0 .

The distributions for systems in the RPR are asymmetric. Precisely at the transition point, $\Gamma = \Gamma_0$, $P(\sigma)$ remains roughly symmetric about the average and the peak remains roughly at the average. However, as Γ increases, the stress at the turning point – i.e., the average σ – increases, but it does so more slowly with Γ than the location of the peak, and the distributions become increasingly asymmetric further above the transition. Precisely at the transition, $P(\sigma)$ is still zero to the left of σ_0 as in the elastic case, but as Γ increases, the region below σ_0 becomes increasingly populated while a shoulder develops immediately to the right of σ_0 . The height of the jump at the shoulder is ≈ 0.1 regardless of Γ or λ . For systems just above the transition with Γ just greater than Γ_0 , there is hardly any mass of $P(\sigma)$ at $\sigma < \sigma_0$ and the jump is relatively sharp. As Γ increases beyond Γ_0 the mass of $P(\sigma)$ at $\sigma < \sigma_0$ slightly increases, smoothing the jump.

The $P(\sigma)$ distributions explain the origin of γ_* and Γ_0 . For the moment, if we ignore the very small mass of $P(\sigma)$ in the creeping regime at $\sigma < \sigma_0$, then, as we load the systems in the reverse direction, $P(\sigma)$ will simply shift to the left until the shoulder reaches the reverse yielding point at $\sigma = -1$. This will occur after a reverse straining by a magnitude of $(1 + \sigma_0)$. Since we start the reverse strain from the turning point at $\gamma = \Gamma$, the value of the strain at the onset of yielding in the reverse direction will occur at $\gamma = \Gamma - (1 + \sigma_0)$. Since this is the onset of plasticity in the reverse direction, we must have that $\gamma_* = (1 + \sigma_0) - \Gamma$ for systems in the RPR. At the critical point, $\Gamma = \Gamma_0$, the onset of plasticity occurs just at the backward turning point, so we must have:

$$\Gamma_0 = \frac{1 + \sigma_0}{2} = 1 - \alpha A_0 - \frac{1}{L^2}. \quad (45)$$

Therefore

$$\gamma_* = \Gamma_0 - (\Gamma - \Gamma_0). \quad (46)$$

In figure 8, we show the ER to RPR transition amplitude, Γ_0 , vs. λ . The dots are the values measured from γ_* vs. Γ curves in the RPR in figure 5 (top) by taking the average of $(\gamma_* + \Gamma)/2$. The solid line is our prediction from the Eshelby kernel using the relation $\Gamma_0 = (1 + \sigma_0)/2$. Independent of λ , the two values match to within symbol size error. As we increase λ , Γ_0 approaches the incompressible limit at 0.36320.

In figure 9, for the $\lambda = 200$ ensemble, we plot the plastic strain accumulated during a backward strain sweep from $\gamma = +\Gamma$ to $\gamma = -\Gamma$. The horizontal axis, $\gamma - \gamma_*$, stands for the magnitude of strain, $\delta\gamma$. The dotted lines are the measured ε as in figure 4 (top). The solid lines are estimates of $\varepsilon - \varepsilon_{p+}$ obtained from $P(\sigma)$ by $(2/L^2)C(\sigma - \sigma_0)$ where C is the cumulative distribution function $C(\sigma) = \int_{-\infty}^{\sigma} P(\sigma') d\sigma'$. The prefactor of $2/L^2$ is the plastic increment resulting from a single flip. Here we neglect the stress redistribution after plastic events, nevertheless, we show that this approximation qualitatively captures the main features of the loading curves. A similar approach was taken in reference [60] to synthetically generate forward and backward loading curves to study mechanical polarization in Lennard-Jones glasses.

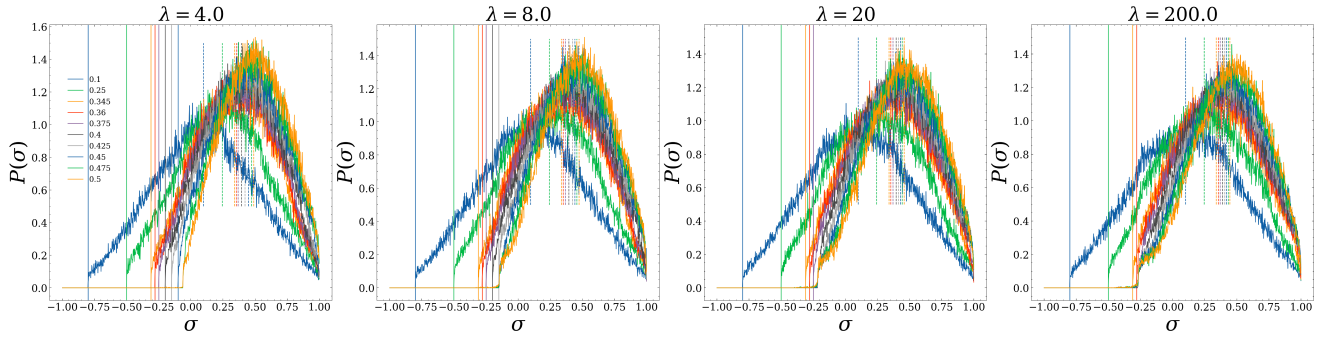


FIG. 7. The distribution of the stress σ at the forward turning point ($\gamma = \Gamma$) in the terminal limit cycles for different cycling amplitudes, Γ . The vertical dashed lines are the averages. The vertical solid lines are at the cutoff values of $\sigma = 2\Gamma - 1$, below which there can be no weight for terminally elastic systems in the ER.

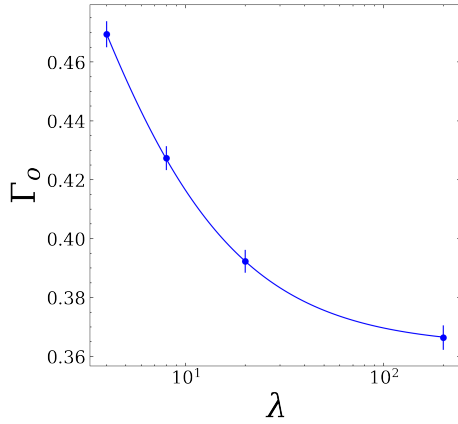


FIG. 8. The transition amplitude, Γ_0 , from the elastic regime (ER) to the reversible plastic regime (RPR) vs. Lamé parameter λ . The solid line is the prediction from the Eshelby kernel using the relation $\Gamma_0 = (1 + \sigma_0)/2$ (equation 45) The dots are measured by averaging $(\Gamma + \gamma_*)/2$ in figure 5 (top) for $\Gamma > \Gamma_0$. The error bars are the standard error of the mean. The dashed line is at the incompressible limit of Γ_0 .

Both the directly measured ε curves and the ones inferred from $P(\sigma)$ show a sharp transition at γ_* that becomes more and more rounded as Γ gets further away from Γ_0 . For instance, the system at $\Gamma = 0.375$ (purple) has essentially no creep and the slope, $\frac{d\varepsilon}{d\gamma}$, jumps from zero to a finite value at γ_* , while for the system at $\Gamma = 0.5$ the transition is smoother. Nevertheless, the slopes above γ_* are relatively insensitive to Γ . Furthermore, for any $\gamma - \gamma_*$, there is more creep the larger $\Gamma - \Gamma_0$. The slopes, $\frac{d\varepsilon}{d\gamma}$, of the actual data and the ones inferred from $P(\sigma)$ are roughly equal. They all start from essentially zero to the left of γ_* and jump to a finite value of 0.2 to the right of γ_* .

V. FORWARD SHEARING

In figure 10, we plot the plastic strain vs. applied strain in forward steady shearing. On the left, we plot the unscaled

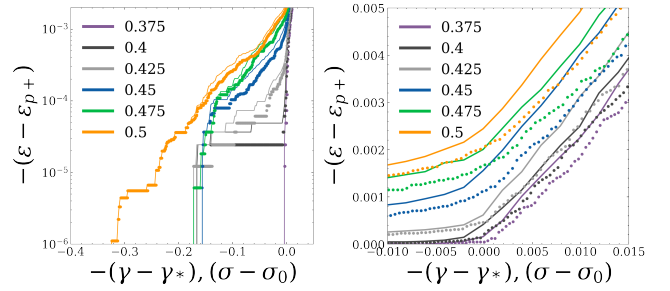


FIG. 9. The plastic strain, ε , vs. $\gamma - \gamma_*$ and $\sigma - \sigma_0$ for $\lambda = 200$. The dots are the measured values of ε as in figure 4 but with the forward plateau value ε^+ subtracted off. The solid lines are estimates of ε obtained from $P(\sigma)$ at the forward turning points as $2/L^2 \int_{-\infty}^{\sigma} P(\sigma') d\sigma'$. The two plots show the same data with different scales and ranges of the axes.

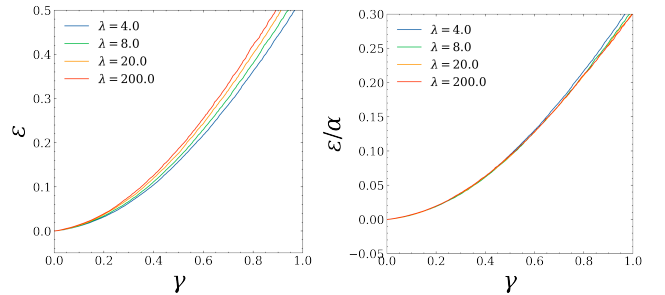


FIG. 10. The plastic strain (ensemble average), ε , vs strain, γ , in forward shear for different values of λ . We subtract off the initial value of ε which is a residual effect of the random quench and scales like $1/L^2$ divided by the number of systems in the ensemble, s all curves begin precisely at zero. The values are sampled at equal increments of strain $\Delta\gamma = 5 \times 10^{-3}$. Right: same curves as on the left after we scale ε by α .

data. We see that the systems with larger λ have higher plastic strain at a given applied total strain. On the right, we scale the plastic strain by the α parameter which controls the amplitude of the stress *redistribution* in the model. The collapse is quite good in the early stages of shearing which shows that the number of shear transformations in a given amount of applied

strain is proportional to α . However, the collapse becomes less accurate at larger strains as the systems begin to approach steady-state shear.

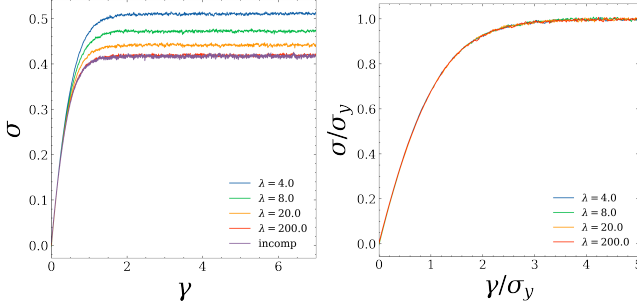


FIG. 11. Left: The shear stress (ensemble average) σ vs. strain γ in forward shear for different values of λ along with the incompressible limit (purple). The stress values are sampled at equal increments of strain $\Delta\gamma = 5 \times 10^{-3}$. Right: same curves as on the left after we normalize both σ and γ by the flow stress, σ_y , in forward shear.

In figure 11 (left), we plot the shear stress (ensemble average)[61], σ , vs. the total strain γ in forward shear. All curves eventually approach a steady state flow stress, σ_y , with a slope of zero. σ_y decreases monotonically with increasing λ . In figure 11 (right), we plot the same curves as in figure 11 (left) but here we normalize both σ and γ by σ_y . The rationale for scaling σ by σ_y is obvious; the rationale for scaling γ by σ_y , is that we know the curves all start with a slope near unity as the plastic strain rate is small initially, and in order to maintain the same slope of unity in all curves, γ must be rescaled by the same amount as σ for any hope of a collapse. Indeed, the curves do collapse remarkably onto a single master curve after the re-scaling. We note that the good collapse of the plastic strain in figure 10 after scaling ε by α but leaving γ unscaled implies that if we were to scrutinize the collapse of the stress in figure 11, we would see a better collapse using α in the early stages rather than σ_y .

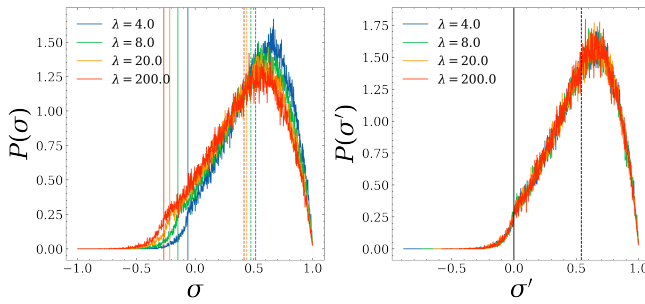


FIG. 12. Left: the distribution of the shear stress $P(\sigma)$ in the steady state of forward shearing for different values of λ . Right: same data on the left but here we perform a coordinate transformation on the stress: $\sigma \rightarrow \sigma' = \frac{\sigma - \sigma_0}{1 - \sigma_0}$. The vertical solid line is at $\sigma'_0 = 0$. The vertical dashed line is the average of σ' over the four distributions: $\sigma'_y = 0.54014$.

In figure 12 (left), we show the shear stress distribution $P(\sigma)$ in the steady state of forward shearing. The solid lines

are at σ_0 . The dashed lines are at the averages. The peaks are located at significantly higher sigma than the averages. $P(\sigma)$ gets increasingly broad with increasing λ pushing both the peak and the average σ to lower values as σ_0 becomes increasingly negative. Reminiscent of the case of cyclic shearing, $P(\sigma)$ has a shoulder around σ_0 resulting from the fact that transforming sites re-enter the distribution precisely at σ_0 .

Motivated by the similar form of the distribution at the shoulder, we make a transformation to a new variable, σ' , where

$$\sigma' = \frac{\sigma - \sigma_0}{1 - \sigma_0} \quad (47)$$

in order to fix the location of the shoulder to $\sigma' = 0$ while leaving the elementary yielding threshold at 1. In figure 12 (right), we plot $P(\sigma')$. After this coordinate transformation, the different distributions in figure 12 (right) are virtually indistinguishable.

In particular, this rescaling tells us that the emergent macroscopic yield stress, σ_y , has a simple dependence on λ . We find that the average σ' value, σ'_y , is essentially independent of λ and equal to 0.54 ± 0.002 (when averaged over our 4 different λ values). This tells us that the yield stress must have the form:

$$\sigma_y = \sigma'_y(1 - \sigma_0) + \sigma_0 \quad (48)$$

$$= \sigma'_y + \sigma_0(1 - \sigma'_y) \quad (49)$$

$$= \sigma'_y + [1 - 2\alpha A_0 - \frac{2}{L^2}][1 - \sigma'_y] \quad (50)$$

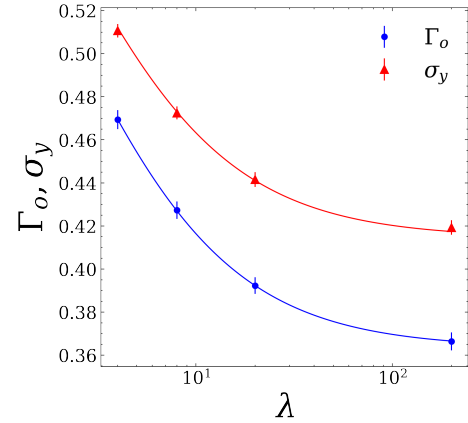


FIG. 13. The flow stress, σ_y , in forward shearing vs. Lame first parameter λ (triangles). We also include Γ_0 reproduced from figure 8 for comparison (dots). The red solid line is σ_y calculated from equation 50

In figure 13, we plot σ_y vs. λ ; and we include Γ_0 from the previous figure for comparison. The triangles are the averages of σ_y measured from the curves in figure 11 in the steady state; where we conventionally define the steady state as $\gamma \geq 2$. The red solid line is σ_y calculated by equation 50 with $\sigma'_y = 0.54$. The two curves have the same trend with λ ; monotonically decreasing with increasing λ . Γ_0 sits below σ_y at all λ values, consistent with our scaling arguments above.

TABLE I. Summary of σ_c , σ_0 , Γ_0 and σ_y expressions provided in the text. Here we ignore terms that are proportional to $\frac{1}{L^2}$.

σ_c	$\approx -\alpha A_0$
σ_0	$\approx 1 - 2\alpha A_0$
Γ_0	$\approx 1 - \alpha A_0$
σ_y	$\approx \sigma'_y + [1 - 2\alpha A_0](1 - \sigma'_y)$

In table V we list the expressions for σ_c , σ_0 , Γ_0 and σ_y . Here we ignore terms that are proportional to $\frac{1}{L^2}$ and we set $\mu = 1$. Again, σ_c is the constrained stress at the origin of solution to the discretized Eshelby problem; where we impose $\varepsilon = 1$ at the origin in an initially stress-free material and solve for the displacement field. σ_0 is the backstress in our model, which is the shear stress at a tile after the tile reach the stress threshold and transforms. Γ_0 is the ER to RPR transition amplitude in cyclic shear. σ_y is the steady state flow shear stress in forward shear. $A_0 = A[0, 0] = 0.317674$. Where, again, $\alpha = 2(\lambda + \mu)/(\lambda + 2\mu) = 2K/(K + \mu)$ as defined in equation 13.

VI. EXPLANATION OF EMERGENT HARDENING BEHAVIOR

For most materials, plastic behavior depends on the history of past deformations. These can tend to harden, soften and polarize the initial material. Whether metal, glass or polymer, strain-hardening is intimately linked to the evolution of the microstructure under deformation: dislocation entanglement, local rearrangements of an amorphous structure, polymer chain alignments, and so on. At the macroscopic level, continuum plasticity models assume ad-hoc hardening laws that prescribe the evolution of the yielding condition – prescribed by the so-called yield surface – during deformation in order to accurately account for experimental results [62].

Interestingly, at the mesoscopic scale, hardening appears to be an emerging property of elasto-plastic models. In Ref. [63, 64], the local plastic thresholds that limit the extent of elastic behavior are drawn from a random distribution. During deformation, it was shown that the gradual exhaustion of weak local plastic thresholds and their replacement by normal thresholds (associated with a new local amorphous structure) induces systematic hardening behavior: the greater the plastic deformation, the higher the macroscopic yield strength. A similar mechanism has recently been invoked to explain the development of a Bauschinger effect in model glasses [60].

In the present model, we identify two distinct hardening regimes. As detailed in previous sections and in Ref. [46], for cycling amplitudes $\Gamma < \Gamma_0$, after a transient, the system locks in onto a perfectly elastic limit cycle devoid of any plastic activity. A discreet symmetry breaking is induced by the choice of initially deforming in the forward sense so that the stress

free residual strain $\delta\Gamma$ is slightly positive. We now define Σ^- and Σ^+ as the negative and positive stress bounds of the elastic range, and $\Delta\Gamma = \Sigma^+ - \Sigma^-$ as its extent. We have immediately:

$$\Sigma^- = -\Gamma + \delta\Gamma, \quad \Sigma^+ = \Gamma + \delta\Gamma, \quad \Delta\Sigma = 2\Gamma \quad (51)$$

Neglecting the slight positive polarization $\delta\Gamma \ll \Gamma$, for cycling amplitudes $\Gamma < \Gamma_0$ we thus recognize an *isotropic* strain hardening behavior: the elastic stress range $[\Sigma^-, \Sigma^+]$ grows almost perfectly symmetrically upon deformation.

For cycling amplitudes beyond the transition, with $\Gamma > \Gamma_0$, we now get a hysteretic limit cycle. We can distinguish between a forward shearing branch and a backward shearing branch, each of which has a pure elastic segment and a plastic segment. We define $\Sigma_{>}^+$ and $\Sigma_{>}^-$ as the stress bounds of the elastic range in the forward shearing branch and $\Sigma_{<}^+$ and $\Sigma_{<}^-$ as the stress bounds of the elastic range in the backward shearing branch. A simple way to summarize our main result above on cycling is that the elastic range

$$\Sigma_{<}^+ - \Sigma_{<}^- = \Sigma_{>}^+ - \Sigma_{>}^- = 2\Gamma_0 \quad (52)$$

is independent of the cycling amplitude. This uniform translation of the region in stress space of elastic stability is the hallmark of *kinematic* hardening laws in continuum plasticity theory.

To illustrate, we introduce a simplified model of the hardening behavior that neglects certain details present in the data we presented above but retains the essential features. First, we neglect the symmetry breaking between forward and reverse shearing and assume that all hysteresis loops are symmetric under $\gamma \rightarrow -\gamma$. Second we suppose that there is absolutely no plastic activity until we reach the yield threshold γ_* . Third, we assume that once the system begins to yield plastically, it flows with a constant plastic strain rate, $\kappa = d\varepsilon/d\gamma$, and that κ is independent of the cycling amplitude. Finally, we assume that in the hysteretic regime, the length of the elastic segments is given precisely by our argument above so that $\gamma_* = \Gamma_0 - (\Gamma - \Gamma_0)$.

Figure 14 shows how these assumptions imply a rather simple behavior. In figure 14a, we plot the plastic strain vs. applied strain for a cycle, in figure 14b, we plot the stress vs. applied strain for a cycle, and in figure 14c, we plot the location of the yield surface, Σ^+ and Σ^- (i.e. the boundary of the elastic regime) vs. the cycling amplitude for both the forward and reverse loading case. For $\Gamma < \Gamma_0$, the ε vs. γ curves are just flat lines at $\varepsilon = 0$, while for $\Gamma > \Gamma_0$, the hysteresis loops are perfectly symmetrical trapezoids with slope zero during elastic loading and slope κ during the plastic flow as can be seen in figure 14a. The amplitude of the hysteresis, ε_p , is then perfectly linear in Γ with $\varepsilon_p = \kappa(\Gamma - \Gamma_0)$. For the stress-strain curves, in figure 14b, we would then have straight lines of slope 1 for the elastic segments and lines with slope $1 - \kappa$ for the plastic flow. In figure 14c, we show the end points of the elastic range $[\Sigma^-, \Sigma^+]$ for both forward and reverse loading.

In the toy model, we set $\kappa = 1/2$ to be consistent with the approximate form of the curves shown above in figure 5. The constant slope of $1/2$ in the toy model explains the approximate slopes of $-1/2$ in the yield stress vs cycling amplitude

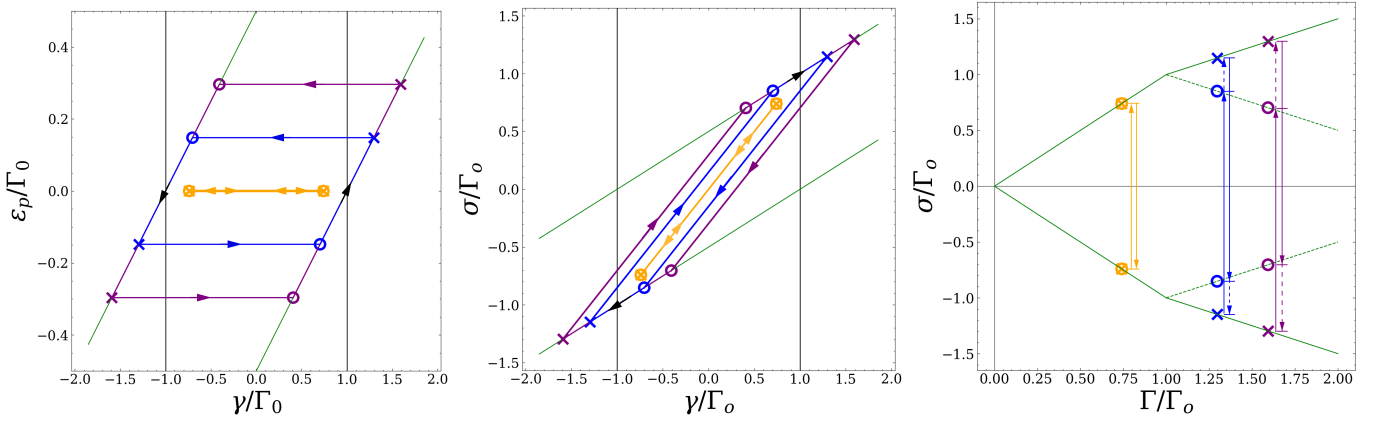


FIG. 14. Simplified model of hysteresis loops and yield surface. a) Plastic strain vs. applied strain at various cycling amplitudes. b) Stress vs. applied strain at various cycling amplitudes. c) Yield surface location, $[\Sigma^-, \Sigma^+]$, in the forward ($[\Sigma_{>}^-, \Sigma_{>}^+]$) and reverse ($[\Sigma_{<}^-, \Sigma_{<}^+]$) driving states. In all plots, crosses indicate the shear reversal points ($\Sigma_{>}^+, \Sigma_{<}^-$), and open circles indicate the yield stress values ($\Sigma_{>}^-, \Sigma_{<}^+$). Gold curve and points corresponds to a typical cycling amplitude below the transition at $\Gamma < \Gamma_0$, and the blue and purple curves correspond to two typical cycling amplitudes above the transition at $\Gamma > \Gamma_0$. Specifically, $\Gamma/\Gamma_0 = 0.74, 1.30, 1.59$, respectively for the gold, blue, and purple amplitudes. a) Plastic strain, ε vs applied strain γ . Solid green lines indicate the idealized hardening behavior with slope $\kappa = 1/2$ that intersect the horizontal axis at $\gamma/\Gamma_0 = \pm 1$. b) Stress, σ vs applied strain, γ . Solid green lines indicate the idealized hardening curve with slope $1 - \kappa = 1/2$ that contain the points $(\sigma/\Gamma_0, \gamma/\Gamma_0) = (1, 1)$ and $(-1, -1)$ respectively. c) Yield stress, $\Sigma_{>}^+, \Sigma_{<}^-$, (dashed green line) and stress at the turning point, $\Sigma_{>}^-, \Sigma_{<}^+$, (solid green line) as a function of cycling amplitude, Γ . Solid blue and purple lines correspond to elastic range in the forward and reverse shearing direction with the sense of the shearing indicated by the arrow heads. Dashed blue and purple lines correspond to the post-yield plastic range.

curves and the approximate slope of $+1/2$ in the hysteresis amplitude vs cycling amplitude curves in figure 5. Of course, the hysteresis curves in figure 4 clearly show that $d\varepsilon/d\gamma$ is not constant, but, rather, increases with strain. Furthermore, this simplified model implies that the hysteresis amplitude is linear in $\Gamma - \Gamma_0$, whereas we showed above that it is a power law in $\Gamma - \Gamma_0$ with an exponent bigger than 1. Nevertheless, for purposes of the present discussion, the main point is that there is a regime below Γ_0 consistent with the isotropic hardening phenomenology of continuum plasticity models, and a regime above Γ_0 consistent with the kinematic hardening phenomenology of continuum plasticity models. In particular, above Γ_0 , the difference between the forward stress at the turning point and the yield stress in the reverse direction is precisely $2\Gamma_0$ – the length of the solid blue and solid purple lines in figure 14c, $\Sigma_{>}^+ - \Sigma_{<}^-$. This shift, in stress space, of the yield surface is precisely the phenomenology which would result from a kinematic hardening law. So it is interesting to note that we observe this transition from isotropic to kinematic hardening behavior precisely at the critical cycling amplitude, Γ_0 .

VII. SUMMARY AND DISCUSSION

In this work, we have explored the behavior of an elastoplastic automaton model of amorphous systems with varying dimensionless compression modulus, K/μ , both under cyclic shear and steady forward shear. The ratio K/μ enters into our model, precisely as in the continuum Eshelby problem, through the ratio $\alpha = 2K/(K + \mu)$. We have shown that, while the magnitude of the elementary macroscopic stress relaxation accompanying a single shear transformation is invariant with respect to α (assuming that the local yielding condition does not depend on K/μ), the stress *redistribution* accompanying that shear transformation in all space including at the yielding site itself, is precisely proportional to α . This has profound implications for the emergent behavior. In particular as K/μ increases, and α increases monotonically toward 2, the Eshelby back stress, σ_0 , becomes increasingly negative. σ_0 , plays a similar role in determining the location of the elastic to reversible-plastic transition in cyclic shearing at a cycling amplitude of Γ_0 as it does in determining the flow stress, σ_y , in forward steady shear. However, the dependence on σ_0 is quantitatively different for Γ_0 than for σ_y , and we were able to explain these quantitative differences in terms of the forms of the $P(\sigma)$ distributions of the local stresses.

In cyclic shearing, for the incompressible case, we have shown in a previous study [22] that the critical amplitude, Γ_0 , is given by $(1 + \sigma_0)/2$, and that for any cycling amplitude with $\Gamma > \Gamma_0$, we have a relatively sharp onset of plasticity at $\gamma_* = \Gamma_0 - (\Gamma - \Gamma_0)$. The plasticity onset is quite sharp at the critical amplitude, Γ_0 , and becomes less sharp at larger Γ with a creeping regime with low plastic strain rate emerging at $\gamma < \gamma_*$. Here, we found the same results for the compressible case after adjusting σ_0 to account for the finite compressibility. This means that Γ_0 decreases with increasing K/μ as σ_0 becomes increasingly negative. The only other adjustment we

needed to make here for the compressible case was to scale the plastic strain amplitude, ε_p , by Γ_0 in order to obtain a collapse for ε_p vs. Γ for different K/μ . The other observations, including the form of the $P(\sigma)$ distributions, go through essentially unchanged.

We have also shown that the shape of the ε vs. γ loading curves near the onset at γ_* can be reasonably well inferred from the $P(\sigma)$ distributions. In particular, the rounding of the loading curves and the creep regime at $\gamma < \gamma_*$ at larger values of $\Gamma - \Gamma_0$ further away from the critical point, were well captured by $P(\sigma)$. The plastic strain inferred from $P(\sigma)$ overestimated, slightly but systematically, the actual values. However, this did not seem to affect the ability to capture the rounding of the loading curves at high $\Gamma - \Gamma_0$. This gives us hope that mean-field approaches based on analysis of the stress distribution without consideration of the spatial structure of the stress field should be able to capture the onset at γ_* and its rounding with the emergence of a creeping regime below γ_* .

In the case of forward steady shear, the loading curves for different K/μ collapse with remarkable precision after rescaling the stress and strain. At early stages for smaller plastic strains, we found a good collapse after rescaling the plastic strain by α , indicating that the incurred plastic strain per unit applied strain is proportional to α . At later stages, on approach to yielding, we used a slightly different scaling where we scaled the stress by the flow stress, σ_y , and we used the scaling properties of $P(\sigma)$ to explain how σ_y depends on K/μ via σ_0 . Similar to the case of cyclic shear, we found that $P(\sigma)$ has a pronounced shoulder at σ_0 . In forward shear, when we transformed to a shifted and scaled value of the stress, $\sigma' = (\sigma - \sigma_0)/(1 - \sigma_0)$, the upper limit of $P(\sigma')$ remained at 1, while the shoulder at σ_0 was mapped to $\sigma' = 0$ for all K/μ . After the transformation, the distributions collapsed almost perfectly. This implied a simple expression for σ_y : $\sigma_y = \sigma'_y + (1 - \sigma'_y)\sigma_0$ where σ'_y is the average of the rescaled universal $P(\sigma')$ distribution which is just a constant. Therefore, as in the case of Γ_0 , σ_y also decreases with K/μ but in a quantitatively different way.

The model we employed here is based on a spatially uniform and fixed-in-time local strain energy function where every site in the system has the same microscopic threshold for yielding at a local elastic strain of unity. A mesoscopic tensorial model (MTM) of crystalline plasticity relying on the construction of an energy density respecting the global symmetry of the Bravais lattice has recently been developed in a close vein [65, 66]. Other so-called elasto-plastic models which have been employed in the literature [8, 46, 47, 57, 64, 67–77] make varying assumptions about the microscopic yielding conditions and the consequences – and temporal dynamics – of a yielding event. One study by Talamali et. al. [64] used a stochastic choice for the plastic strain increment chosen randomly from a uniform distribution with a tunable upper bound. In that study, a similar decrease in the emergent, macroscopic yield stress was observed when the characteristic strain increment was increased as we saw here when increasing α . The motivation in that study to vary the characteristic amplitude of the plastic strain was to make connections to elastic depinning phenomena. In the present study, we were,

rather, motivated to study the consequences of changing dimensionless compressibility, and we were able to precisely rationalize and explain the behavior of both Γ_0 and σ_y , directly in terms of the α parameter and its affects on the $P(\sigma)$ distribution via the Eshelby stress.

Shang et. al. [78] have studied the avalanche behavior in an MD simulation focusing on the transient regime before reaching steady plastic flow. They prepared systems with different quenching protocols resulting in different K/μ and found a pronounced effect of K/μ on the size dependence of the avalanches. Furthermore, they showed a strong dependence on K/μ for the macroscopic stress vs. plastic strain with higher stress at given plastic strain for lower K/μ . However, they did not explore the possible connection between this effect and the amplitude of stress redistribution. It would be interesting to explore this connection further in particle-based models like MD and non-linear elasto-plastic models where the elastic properties do depend on sample age and preparation where proximity to local yielding thresholds generally results in elastically soft spots which become less prevalent in more slowly quenched or annealed systems.

The results we presented here follow from modeling amorphous systems in what we believe to be the simplest possible way with no free parameters other than K/μ . Nonetheless, we believe that the main results, namely the dependence of Γ_0 and σ_y on compressibility, will qualitatively hold in experiments and particle-based simulations (such as molecular dynamics) where local elastic properties and yielding thresholds may vary in space and be distributed more broadly. The main underlying ingredient is the increased amplitude of stress *redistribution* after a yielding event in systems which are less compressible. It would be reasonable to assume that in more realistic models and in experiments, an *effective* α would emerge to set the typical amplitude of stress redistribution. Our findings should motivate future experiments and simulations to have a more precise quantification of the role of compressibility in emergent plastic yielding behavior in cyclic shear and monotonic forward shearing.

It is important to note, that we implicitly work in units of stress and strain that are determined by the elementary yielding strain threshold (conventionally set here to unity). In more realistic models such as MD simulations or in experiments, it would be important to disentangle the effects of changes in *elementary* threshold strains from the Poisson ratio effects we describe here. A simple change in the elementary yield threshold would result in a trivial scaling of the stresses. However, we expect one would see the Poisson ratio effects we see here after appropriately scaling stresses and strains to account for any shifts in the elementary microscopic thresholds.

In mean-field theories of amorphous matter, [79–89], the amplitude of the stress redistribution, along with the distribution from which the stress changes are drawn, plays an important role. In the mean-field approaches, and even other elasto-plastic models constructed in real-space, the amplitude is usually taken as a purely ad-hoc parameter and rarely motivated physically. Here, we show precisely how the amplitude arises from the form of the elastic interactions and how it depends on the elastic moduli. In the model we study here, the

yield condition contains no dependence on pressure or any other field representing any sort of free volume. These dependencies are often invoked in the materials science community [12, 90] to explain the relation between Poisson ratio and ductility. So it is particularly striking that, despite the simplicity of our model, we still see such a strong dependence of the plasticity on the Poisson ratio.

Naturally, there are many more questions remaining to be addressed in future studies. i) Here all systems were prepared in an initial rapid quench. The issue of thermal annealing, or zero temperature aging [47], of the samples before subjecting them to shearing should be investigated. ii) We have used a simple single-amplitude cycling protocol. More complex loading protocols: e.g. small amplitude cycling to anneal mechanically followed by large amplitude cycling to probe yield or more complex protocols would be useful to study. iii) In previous work [46], some of us studied the transition to *irreversible*, diffusive, cyclic shear at a larger transition amplitude, Γ_y , for incompressible systems. A similar study for compressible systems is in order. One might wonder if Γ_y in cycling is equal to σ_y in forward steady shear, or at least has a similar dependence on α . iv) The effect of finite compressibility on the nature of avalanches, both in cycling and steady shear, should be investigated. Properties such as their size distribution, spatial correlations in real space, and finite size effects would be of interest. v) More realistic models with distributions of thresholds and plastic strain increments should be studied [47].

ACKNOWLEDGMENTS

We acknowledge computing support on the Discovery computing cluster at the MGHPC.

-
- [1] A. Argon, *Acta Metallurgica* **27**, 47 (1979).
- [2] M. L. Falk and J. S. Langer, *Physical Review E* **57**, 7192 (1998).
- [3] D. Rodney, A. Tanguy, and D. Vandembroucq, *Modelling and Simulation in Materials Science and Engineering* **19**, 083001 (2011).
- [4] G. Picard, A. Ajdari, F. Lequeux, and L. Bocquet, *The European Physical Journal E* **15**, 371 (2004).
- [5] C. E. Maloney and A. Lemaître, *Phys. Rev. E* **74**, 016118 (2006).
- [6] M. L. Falk and C. E. Maloney, *The European Physical Journal B* **75**, 405 (2010).
- [7] K. E. Jensen, D. A. Weitz, and F. Spaepen, *Phys. Rev. E* **90**, 042305 (2014).
- [8] A. Nicolas, E. E. Ferrero, K. Martens, and J.-L. Barrat, *Rev. Mod. Phys.* **90**, 045006 (2018).
- [9] J. D. Eshelby, *Proceedings of the Royal Society of London. Series A. Mathematical and Physical Sciences* **241**, 376 (1957), <https://royalsocietypublishing.org/doi/pdf/10.1098/rspa.1957.0133>.
- [10] C. R. Weinberger, W. Cai, and D. M. Barnett, “Lecture notes - elasticity of microscopic structures,” (2005).
- [11] T. Mura, *Micromechanics of defects in solids*, 1st ed., Monographs and Textbooks on Mechanics of Solids and Fluids (Martinus Nijhoff, The Hague, Netherlands, 1982).
- [12] C. A. Schuh, T. C. Hufnagel, and U. Ramamurty, *Acta Materialia* **55**, 4067 (2007).
- [13] J. J. Lewandowski, W. H. Wang, and A. L. Greer, *Philosophical Magazine Letters* **85**, 77 (2005).
- [14] J. Schroers and W. I. Johnson, *Physical review letters* **93** **25**, 255506 (2004).
- [15] W. H. Wang, *J. Appl. Phys.* **99**, 093506 (2006).
- [16] G. N. Greaves, A. L. Greer, R. S. Lakes, and T. Rouxel, *Nature Mater.* **10**, 823 (2011).
- [17] D. Richard, M. Ozawa, S. Patinet, E. Stanifer, B. Shang, S. A. Ridout, B. Xu, G. Zhang, P. K. Morse, J.-L. Barrat, L. Berthier, M. L. Falk, P. Guan, A. J. Liu, K. Martens, S. Sastry, D. Vandembroucq, E. Lerner, and M. L. Manning, *Phys. Rev. Mater.* **4**, 113609 (2020).
- [18] A. Barbot, M. Lerbinger, A. Hernandez-Garcia, R. García-García, M. L. Falk, D. Vandembroucq, and S. Patinet, *Phys. Rev. E* **97**, 033001 (2018).
- [19] S. Patinet, D. Vandembroucq, and M. L. Falk, *Phys. Rev. Lett.* **117**, 045501 (2016).
- [20] G. Kapteijns, D. Richard, and E. Lerner, *Phys. Rev. E* **101**, 032130 (2020).
- [21] C. Rainone, E. Bouchbinder, and E. Lerner, *Proceedings of the National Academy of Sciences* **117**, 5228 (2020), <https://www.pnas.org/doi/pdf/10.1073/pnas.1919958117>.
- [22] A. Elgailani, D. Vandembroucq, and C. Maloney, *Phys. Rev. Lett.* **134** (2025).
- [23] M. Lundberg, K. Krishan, N. Xu, C. S. O’Hern, and M. Dennin, *Phys. Rev. E* **77**, 041505 (2008).
- [24] E. D. Knowlton, D. J. Pine, and L. Cipelletti, *Soft Matter* **10**, 6931 (2014).
- [25] N. C. Keim and P. E. Arratia, *Soft Matter* **9**, 6222 (2013).
- [26] N. C. Keim and P. E. Arratia, *Phys. Rev. Lett.* **112**, 028302 (2014).
- [27] N. C. Keim, J. Hass, B. Kroger, and D. Wiekler, *Phys. Rev. Research* **2**, 012004(R) (2020).
- [28] N. C. Keim and J. D. Paulsen, *Science Advances* **7**, eabg7685 (2021).
- [29] N. C. Keim and D. Medina, *Science Advances* **8**, eabo1614 (2022).
- [30] N. C. Keim, J. D. Paulsen, Z. Zeravcic, S. Sastry, and S. R. Nagel, *Reviews of Modern Physics* **91**, 035002 (2019).
- [31] H. Bhaumik, G. Foffi, and S. Sastry, *The Journal of Chemical Physics* **156**, 064502 (2022), <https://doi.org/10.1063/5.0085064>.
- [32] D. Fiocco, G. Foffi, and S. Sastry, *Physical Review E* **88**, 020301(R) (2013).
- [33] P. Leishangthem, A. D. S. Parmar, and S. Sastry, *Nature Communications* **8**, 14653 (2017).
- [34] H. Bhaumik, G. Foffi, and S. Sastry, *Proceedings of the National Academy of Sciences* **118**, e2100227118 (2021), <https://www.pnas.org/doi/pdf/10.1073/pnas.2100227118>.
- [35] N. V. Priezjev, *Physical Review E* **87**, 052302 (2013).
- [36] N. V. Priezjev, *Physical Review E* **93**, 013001 (2016).
- [37] A. Szulc, M. Mungan, and I. Regev, *The Journal of Chemical Physics* **156**, 164506 (2022).
- [38] K. L. Galloway, D. J. Jerolmack, and P. E. Arratia, *Soft Matter* **16**, 4373 (2020).
- [39] I. Regev, T. Lookman, and C. Reichhardt, *Physical Review E* **88**, 062401 (2013).
- [40] I. Regev and T. Lookman, *Journal of Physics: Condensed Matter* **31**, 045101 (2019).
- [41] I. Regev, J. Weber, C. Reichhardt, K. A. Dahmen, and T. Lookman, *Nature Communications* **6**, 8805 (2015).
- [42] E. Schinasi-Lemberg and I. Regev, *Physical Review E* **101**, 023603 (2020).
- [43] I. Regev, I. Attia, K. Dahmen, S. Sastry, and M. Mungan, *Phys. Rev. E* **103**, 062614 (2021).
- [44] M. Mungan, S. Sastry, K. Dahmen, and I. Regev, *Physical Review Letters* **123**, 178002 (2019).
- [45] C. Reichhardt, I. Regev, K. Dahmen, S. Okuma, and C. J. O. Reichhardt, *cond-mat.stat-mech* (2022), [10.48550/ARXIV.2211.03775](https://arxiv.org/abs/10.48550/ARXIV.2211.03775).
- [46] K. Khirallah, B. Tyukodi, D. Vandembroucq, and C. E. Maloney, *Phys. Rev. Lett.* **126**, 218005 (2021).
- [47] D. Kumar, S. Patinet, C. E. Maloney, I. Regev, D. Vandembroucq, and M. Mungan, *The Journal of Chemical Physics* **157**, 174504 (2022), <https://doi.org/10.1063/5.0102669>.
- [48] R. Madariaga, *Bulletin of the Seismological Society of America* **66**, 639 (1976), <https://pubs.geoscienceworld.org/ssa/bssa/article-pdf/66/3/639/5320365/bssa0660030639.pdf>.
- [49] A. R. Levander, *GEOPHYSICS* **53**, 1425 (1988).
- [50] C. Randall, D. J. Scheibner, and P. T. Wu, *Geophysics* **56**, 1757 (1991).
- [51] J. Virieux, *GEOPHYSICS* **51**, 889 (1986).
- [52] R. W. Graves, *Bulletin of the Seismological Society of America* **86**, 1091 (1996),

- <https://pubs.geoscienceworld.org/ssa/bssa/article-pdf/86/4/1091/5343090/bssa0860041091.pdf>.
- [53] M. Schneider, F. Ospald, and M. Kabel, *International Journal for Numerical Methods in Engineering* **105**, 693 (2016).
- [54] W. Press, S. Teukolsky, W. Vetterling, and B. Flannery, *Numerical Recipes 3rd Edition: The Art of Scientific Computing* (Cambridge University Press, 2007).
- [55] S. Merabia and F. Detcheverry, *Europhysics Letters* **116**, 46003 (2016).
- [56] D. F. Castellanos and M. Zaiser, *The European Physical Journal B* **92**, 139 (2019).
- [57] C. Liu, S. Dutta, P. Chaudhuri, and K. Martens, *Physical Review Letters* **126**, 138005 (2021).
- [58] E. E. Ferrero, A. B. Kolton, and E. A. Jagla, *Physical Review Materials* **5**, 115602 (2021).
- [59] M. Popović, T. W. J. de Geus, W. Ji, A. Rosso, and M. Wyart, *Physical Review Letters* **129**, 208001 (2022).
- [60] S. Patinet, A. Barbot, M. Lerbinger, D. Vandembroucq, and A. Lemaître, *Phys. Rev. Lett.* **124**, 205503 (2020).
- [61] Note that large stress drops are present in the automaton dynamics at particular strain values, but we sample the stress and plastic strain at regular strain intervals, so the avalanches are not visible in the stress vs. strain curves.
- [62] A. S. Khan and S. Huang, *Continuum Theory of Plasticity* (Wiley-Interscience, 1995).
- [63] J.-C. Baret, D. Vandembroucq, and S. Roux, *Phys. Rev. Lett.* **89**, 195506 (2002).
- [64] M. Talamali, V. Petäjä, D. Vandembroucq, and S. Roux, *Comptes Rendus Mécanique* **340**, 275 (2012).
- [65] R. Baggio, E. Arbib, P. Biscari, S. Conti, L. Truskinovsky, G. Zanzotto, and O. U. Salman, *Phys. Rev. Lett.* **123**, 205501 (2019).
- [66] R. Baggio, O. U. Salman, and L. Truskinovsky, *Eur. J. Mech. A* **99**, 104897 (2023).
- [67] A. Nicolas, K. Martens, L. Bocquet, and J.-L. Barrat, *Soft Matter* **10**, 4648 (2014).
- [68] K. Martens, L. Bocquet, and J.-L. Barrat, *PHYSICAL REVIEW LETTERS* **106** (2011), 10.1103/PhysRevLett.106.156001.
- [69] J.-C. Baret, D. Vandembroucq, and S. Roux, *Phys. Rev. Lett.* **89**, 195506 (2002).
- [70] K. Karimi, E. E. Ferrero, and J.-L. Barrat, *PHYSICAL REVIEW E* **95** (2017), 10.1103/PhysRevE.95.013003.
- [71] Z. Budrikis and S. Zapperi, *PHYSICAL REVIEW E* **88** (2013), 10.1103/PhysRevE.88.062403.
- [72] Z. Budrikis, D. F. Castellanos, S. Sandfeld, M. Zaiser, and S. Zapperi, *Nature Communications* **8**, 15928 (2017).
- [73] M. Popovic, T. W. J. de Geus, and M. Wyart, *PHYSICAL REVIEW E* **98** (2018), 10.1103/PhysRevE.98.040901.
- [74] B. Tyukodi, D. Vandembroucq, and C. E. Maloney, *PHYSICAL REVIEW E* **100** (2019), 10.1103/PhysRevE.100.043003.
- [75] B. Tyukodi, D. Vandembroucq, and C. E. Maloney, *PHYSICAL REVIEW LETTERS* **121** (2018), 10.1103/PhysRevLett.121.145501.
- [76] B. Tyukodi, S. Patinet, S. Roux, and D. Vandembroucq, *PHYSICAL REVIEW E* **93** (2016), 10.1103/PhysRevE.93.063005.
- [77] J. Lin and M. Wyart, *Physical Review X* **6**, 011005 (2016).
- [78] B. Shang, P. Guan, and J.-L. Barrat, *Proceedings of the National Academy of Sciences* **117**, 86 (2020).
- [79] A. Lemaître and C. Caroli, “Plastic response of a 2d amorphous solid to quasi-static shear : Ii - dynamical noise and avalanches in a mean field model,” (2007), [arXiv:0705.3122](https://arxiv.org/abs/0705.3122) [cond-mat.dis-nn].
- [80] E. Agoritsas, E. Bertin, K. Martens, and J.-L. Barrat, *Eur Phys J E Soft Matter* **38**, 71 (2015).
- [81] E. Agoritsas and K. Martens, *Soft Matter* **13**, 4653 (2017).
- [82] E. E. Ferrero and E. A. Jagla, *Soft Matter* **15**, 9041 (2019).
- [83] J. T. Parley, S. M. Fielding, and P. Sollich, *Physics of Fluids* **32**, 127104 (2020), <https://doi.org/10.1063/5.0033196>.
- [84] J. T. Parley, S. Sastry, and P. Sollich, *Phys. Rev. Lett.* **128**, 198001 (2022).
- [85] E. E. Ferrero and E. A. Jagla, *Journal of Physics: Condensed Matter* **33**, 124001 (2021).
- [86] S. Sastry, *Phys. Rev. Lett.* **126**, 255501 (2021).
- [87] M. Mungan and S. Sastry, *Phys. Rev. Lett.* **127**, 248002 (2021).
- [88] J. O. Cochran, G. L. Callaghan, and S. M. Fielding, “Slow fatigue and highly delayed yielding via shear banding in oscillatory shear,” (2022), [arXiv:2211.11677](https://arxiv.org/abs/2211.11677) [cond-mat.soft].
- [89] J. T. Parley, R. Mandal, and P. Sollich, *Phys. Rev. Mater.* **6**, 065601 (2022).
- [90] Y. Sun, A. Concustell, and A. L. Greer, *Nature Reviews Materials* **1**, 16039 (2016).

Supplemental Material

Finite compressibility and strain hardening in elasto-plastic models of amorphous matter

STAGGERED GRID DISCRETIZATION OF ESHELBY'S PROBLEM

The automaton model we use here is almost identical to the one employed in reference [46]. However, we have changed the details of how the elasticity is discretized. In the present study we have used a so-called staggered grid discretization which is a common procedure in seismology [48–52] and has recently started to see more use in the materials science and theoretical solid mechanics communities [53]. The discretization used here results in precisely the same K_{11} and K_{22} (defined below) as in reference [46], but different K_{12} . The K_{12} used in reference [46] had some pathological behavior which is not present in the staggered grid discretization. Although we do not think these pathologies affected the results in that study or would present any problems in the present study, we nevertheless have opted to use the staggered grid technique here.

We start by defining a displacement field $u_\alpha[I, J]$ on a regular grid with co-ordinates indices I, J . The grid is square with $0 \leq I < L$, $0 \leq J < L$. We define the total strain, ε , from the displacement field using the staggered grid technique [53] and assuming periodic boundary conditions on u so that $u[I + mL, J + nL] = u[I, J]$ for any integers m, n . This gives:

$$\gamma_{xx}[I, J] = u_x[I + 1, J] - u_x[I, J] \quad (\text{S1})$$

$$\gamma_{yy}[I, J] = u_y[I, J + 1] - u_y[I, J] \quad (\text{S2})$$

$$\gamma_{xy}[I, J] = u_x[I, J] - u_x[I, J - 1] \quad (\text{S3})$$

$$\gamma_{yx}[I, J] = u_y[I, J] - u_y[I - 1, J] \quad (\text{S4})$$

For a physical interpretation of this staggered difference scheme, see reference [53]. Note that not all γ fields are derivable from a u field. The γ fields which *are* derived from a u field this way are kinematically compatible within our discretization scheme. We can define a local elastic strain energy as

$$\phi[I, J] = \frac{\mu}{2} ((\gamma_1[I, J] - \varepsilon_1[I, J])^2 + (\gamma_2[I, J] - \varepsilon_2[I, J])^2) + \frac{K}{2} (\gamma_3[I, J])^2 \quad (\text{S5})$$

where μ and K are the shear and compression moduli, γ_1 and γ_2 are the two shear components and γ_3 the dilatant component of the total strain:

$$\gamma_1 = \gamma_{xx} - \gamma_{yy} \quad (\text{S6})$$

$$\gamma_2 = \gamma_{xy} + \gamma_{yx} \quad (\text{S7})$$

$$\gamma_3 = \gamma_{xx} + \gamma_{yy} \quad (\text{S8})$$

and ε_1 and ε_2 are two prescribed plastic strain fields or so-called eigenstrains. The total elastic strain energy is then simply a sum over the lattice.

$$\phi = \sum_{IJ} \phi[I, J] \quad (\text{S9})$$

The discretized Eshelby problem is then to find a displacement field and the associated strain field which minimizes ϕ subject to the prescribed ε_1 and ε_2 . Note that posing the minimization problem in terms of displacements automatically ensures the resulting strain field is kinematically compatible. If the prescribed ε field happens to be compatible, then the solution will be trivial with $\gamma = \varepsilon$, but we are typically interested in incompatible ε fields. Because of the linearity of the problem, we can express the solution for any arbitrary prescribed ε_1 and ε_2 fields in terms of the solution to a unit delta source,

$$\varepsilon_1[I, J] = \delta_{I,0} \delta_{J,0} \quad (\text{S10})$$

and

$$\varepsilon_2[I, J] = \delta_{I,0} \delta_{J,0}. \quad (\text{S11})$$

Note that these delta source fields are not kinematically compatible and could not have been derived from any displacement field. We define the strain fields derived from the displacements resulting from the energy minimization problem with a delta source as $K_{11}, K_{12}, K_{21}, K_{22}$ where: K_{11} is the γ_1 strain resulting from an imposed ε_1 eigenstrain, K_{12} is the γ_1 strain resulting from an imposed ε_2 eigenstrain, K_{21} is the γ_2 strain resulting from an imposed ε_1 eigenstrain, and K_{22} is the γ_2 strain resulting from an imposed ε_2 eigenstrain. We specialize here to the incompressible limit where $K/\mu \rightarrow \infty$. The solution to this energy minimization problem is most easily expressed in Fourier space.

$$\tilde{K}_{11}[p, q] = -\frac{4q_x - q_{x+} - q_{y-} - q_{y+}}{\mathcal{D}} = -\frac{4\Delta_x^2 \Delta_y^2}{\mathcal{D}} \quad (\text{S12})$$

$$\tilde{K}_{22}[p, q] = -\frac{(q_x - q_{x+} - q_{y-} - q_{y+})^2}{\mathcal{D}} = -\frac{(\Delta_x^2 - \Delta_y^2)^2}{\mathcal{D}} \quad (\text{S13})$$

$$\tilde{K}_{12}[p, q] = \frac{2q_{x+} + q_{y+} (q_x - q_{x+} - q_{y-} - q_{y+})}{\mathcal{D}} = \frac{2q_{x+} + q_{y+} (\Delta_x^2 - \Delta_y^2)}{\mathcal{D}} \quad (\text{S14})$$

$$\tilde{K}_{21}[p, q] = \frac{2q_x - q_{y-} (q_x - q_{x+} - q_{y-} - q_{y+})}{\mathcal{D}} = \frac{2q_x - q_{y-} (\Delta_x^2 - \Delta_y^2)}{\mathcal{D}} \quad (\text{S15})$$

where

$$\Delta_x^2 = q_{x+} + q_{x-} \quad (\text{S16})$$

$$\Delta_y^2 = q_{y+} + q_{y-} \quad (\text{S17})$$

are the Fourier transforms of the second ordered centered difference operators in the x and y direction and where

$$\mathcal{D} = (\Delta_x^2 + \Delta_y^2)^2 \quad (\text{S18})$$

is the Fourier transform of the the graph Laplacian of the graph Laplacian, and where

$$q_{x+}[p, q] = -i(+\exp[+2\pi ip/L] - 1) \quad (\text{S19})$$

$$q_{x-}[p, q] = -i(-\exp[-2\pi ip/L] + 1) \quad (\text{S20})$$

$$q_{y+}[p, q] = -i(+\exp[+2\pi iq/L] - 1) \quad (\text{S21})$$

$$q_{y-}[p, q] = -i(-\exp[-2\pi iq/L] + 1) \quad (\text{S22})$$

$$(\text{S23})$$

are the Fourier transforms of the forward and backward difference operators in the x and y directions. We have used the discrete Fourier transform conventions:

$$\tilde{K}[p, q] = \left(\frac{1}{\sqrt{L}}\right)^2 \sum_{I, J} K[I, J] \exp[+2\pi(Ip + Jq)/L] \quad (\text{S24})$$

$$K[I, J] = \left(\frac{1}{\sqrt{L}}\right)^2 \sum_{p, q} \tilde{K}[p, q] \exp[-2\pi(Ip + Jq)/L] \quad (\text{S25})$$

With the solution for the delta sources, we can then write the solution for an arbitrary source field in terms of a convolution:

$$\gamma_1[I, J] = \sum_{IJ} K_{11}[M - I, N - J] \varepsilon_1[M, N] + K_{12}[M - I, N - J] \varepsilon_2[M, N] \quad (\text{S26})$$

$$\gamma_2[I, J] = \sum_{IJ} K_{21}[M - I, N - J] \varepsilon_1[M, N] + K_{22}[M - I, N - J] \varepsilon_2[M, N] \quad (\text{S27})$$

Then, of course, because of the convolution theorem, we have a decoupled mode-wise relation in for each p, q mode in Fourier space,

$$\tilde{\gamma}_1[p, q] = \tilde{K}_{11}[p, q] \tilde{\varepsilon}_1[p, q] + \tilde{K}_{12}[p, q] \tilde{\varepsilon}_2[p, q] \quad (\text{S28})$$

$$\tilde{\gamma}_2[p, q] = \tilde{K}_{21}[p, q]\tilde{\epsilon}_1[p, q] + \tilde{K}_{22}[p, q]\tilde{\epsilon}_2[p, q] \quad (\text{S29})$$

Our expressions for K were obtained by differentiating the energy with respect to u_x and u_y , solving the linear equations for the u fields which give zero energy derivative and then re-inserting those u fields back into the staggered difference scheme to find γ , and we have not shown those steps here as they are straightforward but tedious. We note that the present \tilde{K}_{11} and \tilde{K}_{22} are *precisely* the same as in reference [46] and as in the continuum Eshelby problem [4]. It is only \tilde{K}_{12} and \tilde{K}_{21} which are different in the present staggered-difference scheme. The definition of the automaton from a piece-wise quadratic strain-energy function and the initialization procedure are then precisely as in reference [46] so we do not elaborate further here.